Bachelorthesis

Detection of Rydberg-states of electrons on helium confined in μ-channels

submited from

Sebastian Grossenbach

at the

Universität Konstanz

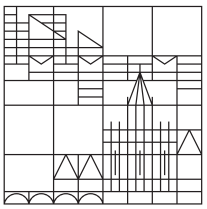

Mathematisch-Naturwissenschaftliche Sektion
Fachbereich Physik

Reviewer

Prof. Dr. Paul Leiderer
Prof. Dr. Denis Konstantinov

Konstanz, 23. Mai 2019

German Abstract

In dieser Arbeit wird die Rydberg-Detektion von Elektronen auf Helium in Mikrokanälen durch Finite-Elemente-Modellierung (FEM) untersucht und der Versuchsaufbau für die experimentelle Realisierung der Rydberg-Detektion in Mikrokanälen entwickelt.
In dem Modell der FEM wird die Reduktion des Heliums in den Mikrokanälen aufgrund der Van-der-Waals-Anziehung, im Gegensatz zu früheren Arbeiten, berücksichtigt. Das Modell dient zur Auslegung des Probendesigns - vor allem eingeschränkt durch die begrenzte Mikrowellenfrequenz von 400 GHz. 4 µm tiefe und 20 µm breite Kanäle erfüllen dieses Kriterium. Der Einfluss unterschiedlicher Füllhöhen auf das elektrische Haltefeld wird analysiert.
Um eine Kanaltiefe von 4 µm zu erreichen, werden die Eigenschaften des Photoresists ARN 4450-10 charakterisiert und die bestehende Probenherstellung auf diesen Photoresists als Isolierschicht abgestimmt. Eine Probenzelle und eine PCB als Probenhalter werden entworfen und zusammengebaut. Die Proben werden in einer vorhandenen Probenzelle geprüft und die Deposition von Elektronen auf der He-Oberfläche in den Kanälen demonstriert. Außerdem wird die grundlegende Kontrolle des Elektronensystems durch die Gate-Spannung V_{GA} und die Channel-Spannung V_{CH} demonstriert.

Contents

1 Abstract

In this work the Rydberg-detection of electrons on helium in microchannels is studied by finite element modeling (FEM) and the experimental set up is developed for the experimental realization of the Rydberg-detection in micro channels.
In the model of the FEM the depression of the Helium in the micro channels due to Van der Waals attraction, in contrast to previous works, is considered. The model is used to determine the design of the sample - mostly restricted by the limited micro wave frequency of 400 GHz. 4 µm deep and 20 µm wide channels are found to satisfy the requirements. The influence of different filling levels on the holding field is analyzed.
To achieve a channel depth of 4 µm the dependence of the thickness on the spin rate, as well as the chemical stability against the solvents and developer used in later steps of the fabrication of the photoresist ARN 4450-10 are investigated and the existing sample fabrication adjusted for this photoresist as insulating layer. A sample cell and PCB as sample holder are designed and assembled. The samples are checked in a existing sample cell and the deposition of electrons on the He surface in the channels is demonstrated. Also, basic control of the electron system by the gate voltage V_{GA} and channel voltage V_{CH} is demonstrated.

2 Acknowledgement

I wish to thank all the people who helped to complete this project. Foremost, I want to express my gratitude to my supervisor Prof. Denis Konstantinov at the Okinawa Institute of Science (OIST) and Technology for offering me the opportunity to do the bachelor thesis in the quantum dynamics unit and his continuous support through out the project. Furthermore, I want to pay my special regards to Prof. Paul Leiderer for supervising the bachelor thesis in Konstanz and helping me, to get in touch with Prof. Denis Konstantinov.
I want to thank everyone of the Quantum Dynamics Unit for the great talks and teaching me many different things. especially, I want to thank Shan Zou for helping with the simulations, cleanroom work and also plenty lifts back home after missing the last bus due to working late. I also want to thank Emil Joseph for explaining how to run the ^{3}He refrigerator and supporting me in running it. Additionally I want to thank Oleksiy Zadorozhko for all the help regarding mechanical engineering such as making the waveguides, hard-soldering holes and also explaining the handling of the ^{3}He-^{4}He dilution refrigerator.
For the help with the application for PROMOS of the DAAD and the internship at the OIST I want to thank Susanne Sprenger. I also want to thank her also for the great feedback on the EIH 2020 poster. For the invitation to this conference in Bangaluru I want to thank Prof. Amberish Ghosh.
Finally, I want to thank the DAAD for the financial support via PROMOS and also the OIST for the financial support.

3 Introduction

Quantum computing is treated as one of the key technologies for the future. Various systems are explored as candidates for future quantum processors such the solid state quantum bits based on Josephson-junctions, quantum dots, cold atoms/ions, nitrogen-vacancy centers in diamond and others. Even though quantum supremacy has been shown with quantum bits based on Josephson-junctions [1], many problems arise in a solid state quantum bit due to intrinsic defects and impurities of the material. This makes it impossible to make perfectly identical quantum bits.
The system of electrons on the surface of liquid Helium is intrinsically pure and free of defects. Therefore, the use of electrons on the surface of liquid Helium for quantum computing has been proposed 1999 by Platzman and Dykmann [2]. Also other approaches with electrons on Helium have been proposed [3]. In all these approaches, electrons are confined in a patterned substrate or channels and the quantum bit operations depend on the Rydberg-excitation of a single electron in vertical direction.
The transport properties and precise control of electrons in channels is investigated and the Rydberg-excitation for electrons on the surface of bulk helium is demonstrated [4]. This project will contribute to the precise control and manipulation of electrons on Helium for later use in quantum computing. It is also not clear yet how the transport behavior in a quasi one dimensional confinement is affected by Rydberg-excitation.
In this thesis we plan to develop a electrostatic model to calculate the microwave frequency needed for Rydberg-excitation and also design and fabricate a microchannel device to test the results obtained by the model.

4 Theoretical Background

This chapter will start with a description of the quantized states of surface state electrons including the influence of the electric holding field on the transitions between different Rydberg states. Then the general theoretical framework of electric transport in strongly-correlated systems will be reviewed in section 4.2. On the basis of this the two governing scattering mechanisms (vapor and ripplon scattering) will be discussed in section 4.3. Especially the effect of the Rydberg-excitation from the ground level to an excited state will be evaluated and discussed in context of the current state of studies. The final section 4.4 will focus on the Wigner-cristallization and the Bragg-Cherenkov scattering.

4.1 Bound Electrons on the Surface of Liquid Helium

Electrons bound to the surface of liquid helium (He) form a stable system. In a simplified model we consider an electron with charge $-e\,(\,e>0)$ at distance z above the surface of the liquid He. As the nuclear charge of the He-ion is $2e$, there are 2 electrons bound to the He atom. These electrons occupy the $1s$ orbitals. Due to the Pauli exclusion principle, an additional electron must occupy orbitals with higher energy, which leads to a strong repulsion between electrons and He atoms. This repulsion creates a potential barrier of V_0 =1 eV, which keeps the electrons from entering the liquid He [5][6].
Additionally there is a long range attraction between the liquid He and the electron. Due to the electric field of the electron the liquid helium is polarized. This polarization causes an electric field, which exerts an attractive force onto the electrons. The combination of the short range repulsion with the long range attraction is responsible for the bound surface states of electrons on the surface of liquid He.
Considering a flat unconfined liquid He surface, one can solve the Poisson equation by introducing an image charge q_i (analogous to the calculations at metal-vacuum interfaces) at position $-z$. In the dielectric material the polarization leads to a small compensation of the electric field, while in metals the electric field is fully compensated. Therefore the image charge q_i in a dielectric material is smaller compared to the one in metals, with $q_i = +e\frac{\epsilon_{\mathrm{He}}-1}{\epsilon_{\mathrm{He}}+1} = +e\Lambda$ and the permittivity of He $\epsilon_{\mathrm{He}} = 1.056$. With an additional electric field normal to the surface $E_\perp$ the potential energy of the electron can be approximated as

$$U(z) = V_0\theta(-z) - \frac{\Lambda}{z+z_0}e^2\theta(z) + eE_\perp z, \tag{4.1}$$

where $\theta(z)$ is the unit side step function. To avoid singularity in the image charge potential the parameter z_0 is introduced [7]. It is in the order of a typical atomic scale (1 Å) and shifts the

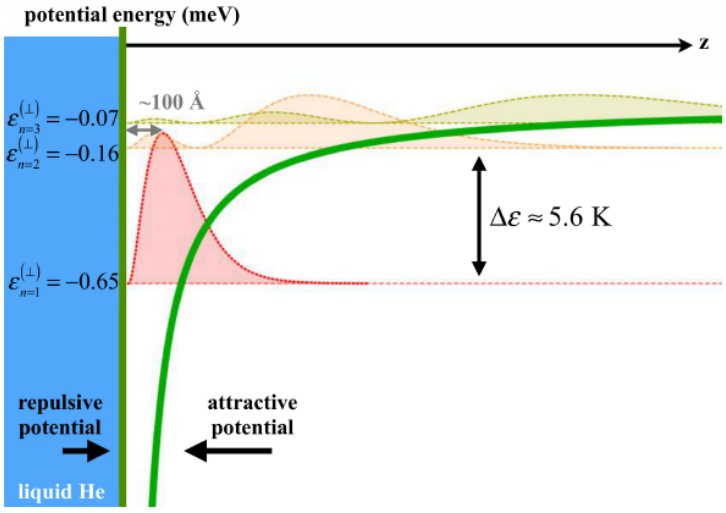

Figure 4.1: Probability density of SSE eigenstates without electric field $E_\perp$: The eigen-energies and probability densities for the first three eigenstates of a single SSE are shown in the image potential.The figure is taken from [8].

singularity beyond its interaction range. Because the typical eigen-energies of a electron trapped in this potential are much smaller than V_0, it is sufficient for the following discussion to simplify the model with $V_0 \to \infty$ and $z_0 \to 0$. With $E_\perp = 0$ the corresponding 1D Schrödinger equation yields to the one describing the radial motion of an electron in the hydrogen atom. Therefore, the quantized energy levels along the z axis of the SSE are

$$\epsilon_n^{(\perp)} = -\frac{\Lambda R_y}{n^2} \approxeq -\frac{0.65}{n^2}\text{meV} \approxeq -\frac{7.5}{n^2}K, \tag{4.2}$$

where $R_y = 13.6\,\text{eV}$ is the Rydberg constant. Due to this reduction of the eigen-energies with Λ compared to the hydrogen atom, also the transition frequencies are reduced. Therefore, the transition frequencies are no longer in the visible/UV range, but the microwave range with $(\epsilon_2^{(\perp)} - \epsilon_1^{(\perp)})/\hbar \approxeq 119.2\,\text{GHz}$ and $(\epsilon_3^{(\perp)} - \epsilon_1^{(\perp)})/\hbar \approxeq 141.3\,\text{GHz}$. The corresponding wave-functions are

$$\psi_n(z) = R_{n0}(z) * z, \quad n \in \mathbb{N}\,, \tag{4.3}$$

where R_{n0} are the equations for the radial wave functions of an electron in the hydrogen atom with angular momentum $l = 0$. The potential as well as the probability densities for the $n = 1,2,3$-states are shown in figure 4.1. One can easily see that for higher exited states the average height $\langle n|z|n\rangle$ of the electron above the surface increases. For the first and second states is $\langle 1|z|1\rangle \approxeq 114\,\text{Å}$ and $\langle 2|z|2\rangle \approxeq 456\,\text{Å}$ respectively.

In the case of the experiments conducted here, an electric field is applied normal to the surface. For small electric fields it can be taken into consideration as a small perturbation using usual perturbation theory:

$$\delta\epsilon_n^{(\perp)} \approxeq eE_\perp\langle n|z|n\rangle\,. \tag{4.4}$$

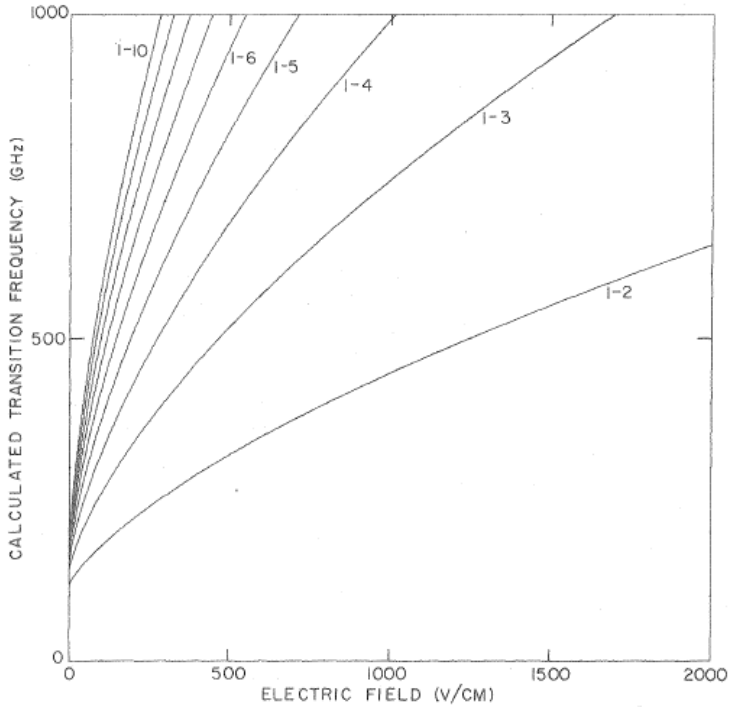

Figure 4.2: Transition frequencies from the ground state to the excited states. As expected the transition frequencies increases with the electric field. The graph is taken from [9].

This describes a linear Stark shift for the SSE states. Due to the proportionality to the average height $\langle n|z|n\rangle$, higher states are stronger affected by the energy shift. Therefore, the Stark shift increases the transition frequencies between the ground state and exited states.

For stronger electric field the perturbation theory breaks down and the corrections become non-linear terms of $E_\perp$. In the limit of sufficiently large holding fields ($E_\perp \gg \frac{\Lambda e}{z_0}$, the image potential can be disregarded. The resulting potential is a triangular-shaped potential with eigenvalues

$$\epsilon_n^{(\perp)} = eE_\perp \frac{\zeta_n}{\gamma_F}, \quad \gamma_F = \left(\frac{2m_e eE_\perp}{\hbar^2}\right)^{1/3}, \tag{4.5}$$

where ζ_n the n-th zero of the Airy-function with $\mathrm{Ai}(-\zeta_n) = 0$. The corresponding wave-functions are

$$\psi_n(z) = \text{constant} \times \mathrm{Ai}\left[\left(z - \frac{\epsilon_n^{(\perp)}}{eE_\perp}\right)\gamma_F\right], \tag{4.6}$$

where the constant term is chosen to satisfy the normalization condition. For a pressing field of $1000\,\mathrm{V\,cm^{-1}}$ the average heights are $\langle 1|z|1\rangle \approxeq 114\,\text{Å}$ and $\langle 2|z|2\rangle \approxeq 268\,\text{Å}$.

To calculate the transition frequency for moderate holding fields $E_\perp$, a numerical integration of the Schrödinger equation resulting from the potential (4.1) was performed by Lambert [9]. The result is shown in figure 4.2. In the limit of weak and strong holding fields the linear increase of the transition frequency with $E_\perp$ is clearly visible. In an intermediate region the slope is non-linear, but still increasing monotonously.

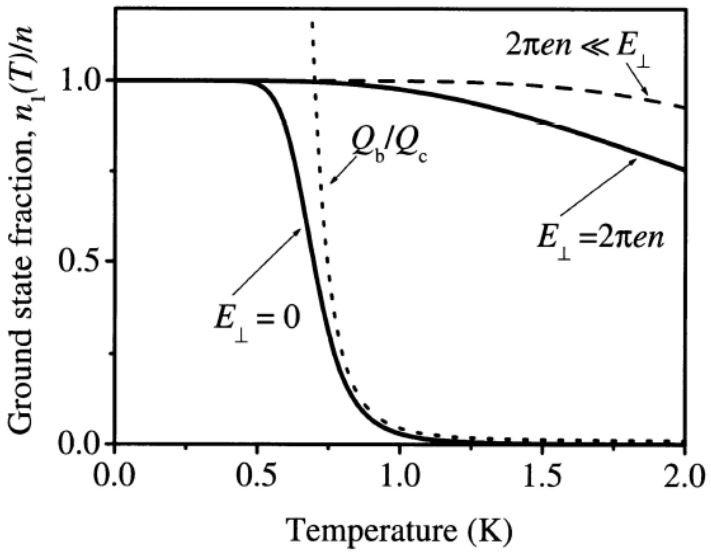

Figure 4.3: Population of the ground state: Population of the ground surface level under different conditions concerning the holding electric field and electron densities. The ratio Q_b/Q_c, where Q_b and Q_c are the partition functions of the ground state $Q_b = \sum_{n=1}^{\infty} e^{\epsilon_n^{(\perp)}/T}$ and continuous spectrum state $Q_c = \sqrt{\frac{m_e T}{8\pi\hbar^2}} L_z$ with container length L_z, is drawn in the dotted curve for the condition $E_\perp = 0$. The population of the ground state is calculated according to $\frac{n_1}{n} = \frac{\exp(\epsilon_n^{(\perp)/T})}{\sum_n \exp(\epsilon_n^{(\perp)/T})}$ using the Maxwell-Boltzmann-distribution. The figure is taken out of [8], reproduced from [10].

The binding energy of the ground state and the energy difference between different eigen-states increases in the presence of $E_\perp$. As a consequence, also the population of the ground state increases with $E_\perp$. In typical experimental conditions ($T \approx 0.8\,\mathrm{K}$ & $E_\perp$ present) the fractional population without excitation using microwaves is almost 1.

4.2 Transport Theory for Electrons

In the experiments we measure the effect of a driving force on the motion of the whole electron system. The relation of the motion with drift velocity $\vec{v}_d$ and the external driving field $\vec{F}_{ex} = e\vec{E}$ is obtained in the semi-classical Boltzmann transport equation (BTE). The change in the distribution function of particles in phase space $f = f(\vec{r},\vec{p},t)$ is due to stochastic scattering processes

$$\frac{\mathrm{d}f}{\mathrm{d}t} = \left(\frac{\partial f}{\partial t}\right)_{\text{collision}} . \tag{4.7}$$

Expressing $\frac{\mathrm{d}f}{\mathrm{d}t}$ in all the derivatives for $\vec{r}$,$\vec{r}$ and t yields

$$\frac{\partial f}{\partial t} + \frac{\vec{p}}{m} \cdot \nabla_r f + \vec{F} \cdot \nabla_p f = \left(\frac{\partial f}{\partial t}\right)_{\text{collision}} . \tag{4.8}$$

Assuming the system is in the stationary state ($\frac{\partial f}{\partial t} = 0$) and uniform density ($\nabla_p \cdot f$) the equation (4.8) can be simplified to

$$\vec{F} \cdot \nabla_p f = \left(\frac{\partial f}{\partial t}\right)_{\text{collision}} . \tag{4.9}$$

The collision term is the most interesting though. It is evaluated in the relaxation time approximation, which can be expressed as

$$\left(\frac{\partial f}{\partial t}\right)_{\text{collision}} = -\frac{f(\vec{p}) - f_{\text{eq}}(\vec{p})}{\tau(\vec{p})} , \tag{4.10}$$

where $\tau(p)$ represents the relaxation time. Then the distribution function is

$$f(\vec{p}) = f_{\text{eq}}(\vec{p}) - e\tau(\vec{p})\vec{E} \cdot \nabla_p f(\vec{p}) . \tag{4.11}$$

The electrical current density can be deducted by expanding the distribution function in powers of the electric field. Taking only the terms up to the first order into consideration this yields

$$J_a = \frac{e}{V} \int \mathrm{d}r^3 \int \frac{\mathrm{d}p^3}{(2\pi\hbar)^3} f v_a = \sum_{b=1}^{3} \sigma_{ab} E_b , \tag{4.12}$$

where σ_{ab} is the conductivity tensor. For a quantum Fermi gas, $f_{\text{eq}} = \frac{1}{e^{(\epsilon-\epsilon_F)/k_B T}+1}$, equation (4.12) represents Ohm's law. In the stationary state the force of the driving field and the stochastic scattering events are in balance and result in a constant drift velocity v_d of the electronic system.

4.3 Scattering

There are three main scattering mechanism in the SSE system: scattering with vapor, scattering with rippplons and electron-electron scattering. Ripplons are quantized capillary waves of the superfluid He. The number of vapor atoms and ripplons decreases with cooling. Therefore, the scattering rate decreases leading to a higher mobility along the surface. Measured Data is shown in figure 4.4. While scattering with the background scatters is connected with a momentum change of the SSE-system, the total momentum is conserved in electron-electron scattering. Because of that reason, electron-electron scattering will not be discussed in further detail. Still, the electron-electron scattering is important, especially to bring the SSE-system into thermal equilibrium.

4.3.1 Scattering with Vapor Atoms

The scattering with vapor atoms is only short-ranged. The density of the vapor atoms above the surface varies exponentially with temperature

$$n^{(a)}(T) = \left(\frac{M_a T}{2\pi\hbar^2}\right)^{3/2} \exp\left(-\frac{Q}{T}\right) , \tag{4.13}$$

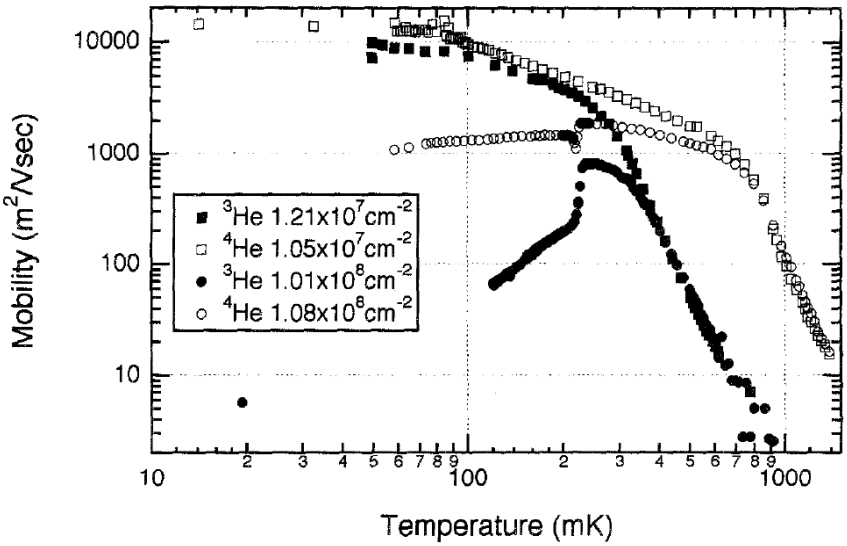

Figure 4.4: Comparison of $\mu_{^3He}$ and $\mu_{^3He}$ as function of temperature: The temperature dependence of $\mu_{^3He}$ and $\mu_{^3He}$is qualitativily the same, just shifted to lower temperatures for $\mu_{^3He}$ because of the higher vapor pressure of ^{3}He. The figure is taken from [11].

where Q is the evaporation constant and M_a is the mass of the helium atom. Therefore, the electron mobility μ decreases exponentially with temperature

$$\mu = \frac{8ea_0}{3\pi\hbar An^{(a)}} \propto T^{-3/2} \exp\left(\frac{Q}{T}\right) , \tag{4.14}$$

where a_0 is the effective Bohr radius of the SSE and A the scattering crossection of the vapor atom [12]. To describe the density profile of He^4 vapor $\rho(z)$ Lurio [13] used a function, of which the derivative is given by an asymmetrical hyperbolic secan-function with

$$\begin{aligned} \frac{\mathrm{d}n^{(a)}(z)}{\mathrm{d}z} &= \frac{C}{\exp(az) + \exp(-bz)} \\ a = \frac{1+\exp(-\nu)}{2\sigma_0} \quad b &= \frac{1+\exp(\nu)}{2\sigma_0} , \end{aligned} \tag{4.15}$$

with $\nu = -1.1$ reflecting the asymmetry of the interface and $\sigma_0 = 1.97\,\text{Å}$ at $1.13\,\text{K}$ as measure for the interface width. Since the average distance between the surface of the Helium and the electrons in the ground state is more than $100\,\text{Å}$, we can disregard the term $\exp(-bz)$ in equation (4.15) simplifying it to

$$\frac{\mathrm{d}n^{(a)}(z)}{\mathrm{d}z} = C\exp(-az) . \tag{4.16}$$

Therefore, the density of vapor atoms and, hence, also the scattering frequency depends exponentially on the distance leading to a much lower scattering rate for excited states. The simple two-level approach with ground state and first excited state for the SSE conductivity limited by vapor atom scattering [14] predicts a decrease in SSE resistivity by 10%.

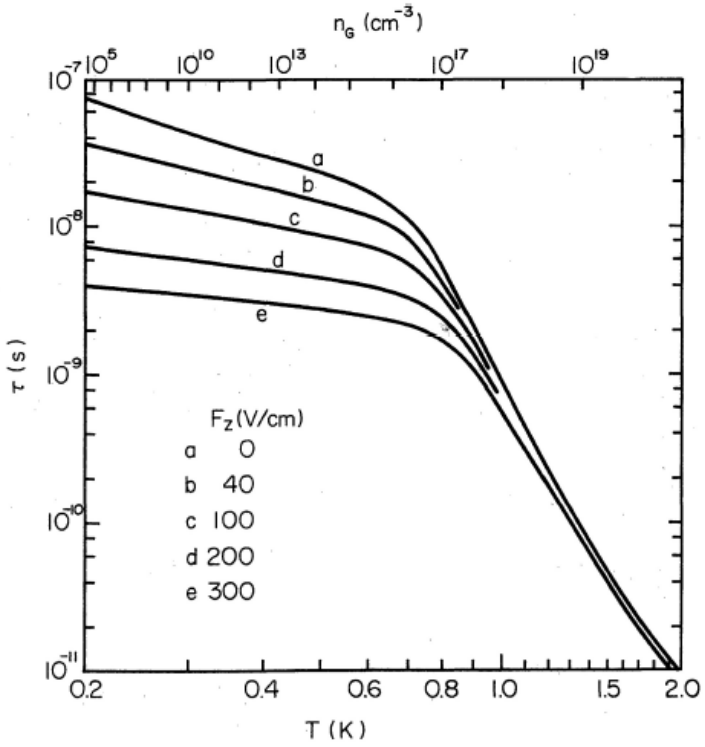

Figure 4.5: Momentum relaxation time τ as function of temperature for various pressing fields F_z: For $T < 0.7K$ the ripplon scattering becomes dominant and shows a slow (linear) increase with decreasing temperature. The dependence on the pressing field is significant. The figure is reproduced from [10]

4.3.2 Scattering with Ripplons

At low temperatures $T < 0.7K$, the vapor density is extremely low and therefore the scattering with ripplons dominates. The number of ripplons is described by the Bose-Einstein distribution. Due to the thermal wave number $k \approx 2k_T = \sqrt{8m_eT}/\hbar$ of the SSE is much smaller than the thermal ripplon wave number q_T, only low energy ripplons with $q \leq 2k$ are involved in the momentum relaxation. For ripplons with energy $\hbar\omega_q \ll k_BT$ the dispersion relation is $\omega_q = \sqrt{\alpha/\rho}q^{3/2}$. The corresponding density of ripplons involved in scattering decreases linearly with temperature [10]

$$n_q^{(r)}(T) = \frac{1}{\exp\left(\frac{\hbar\omega_q}{k_BT}\right)} \simeq \frac{k_BT}{\hbar\omega_q}\,. \tag{4.17}$$

Therefore, also the electron-ripplon scattering rate decreases linearly with T.

To describe the electron scattering by ripplons, the surface displacement operator $\xi(r)$ of the ripplons is introduced. It is entering the polarization interaction potential of the electron with the helium. As seen in graph 4.5, the electron-ripplon scattering is strongly affected by the pressing field $E_\perp$. This can be explained by the change of probability distribution near the surface through the pressing field. For large $E_\perp$ the coupling of electrons and ripplons increases and therefore the SSE mobility decreases [12][15]. For higher excited states the probability distribution close to the surface decreases, therefore one expects an increase in SSE mobility [14]. Because the wave function of the bound electron should be zero at the helium-vapor interface the coupling term

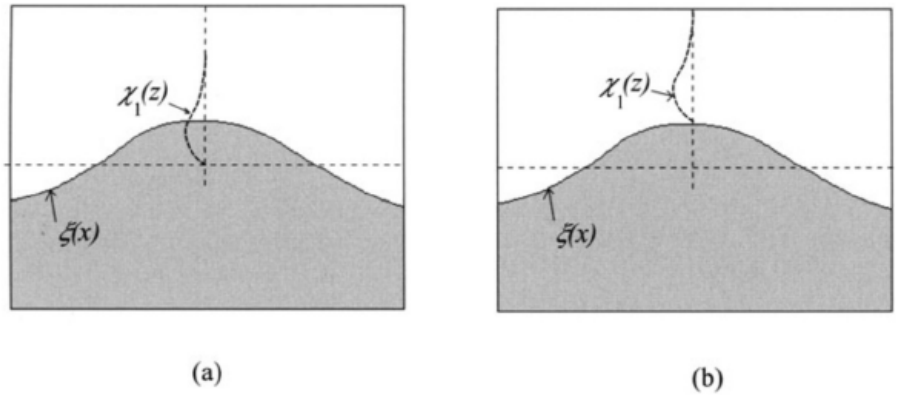

Figure 4.6: Single SSE on a uneven surface: The diagram shows the difference in the polarization interaction of electrons which do not follow the interface displacement (a) and for bound electrons (b). The figure is reproduced from [10].

of the electron-ripplon interaction is linearly proportional to $E_\perp$ [10]. Consequently the electron should follow the surface displacement of the ripplon which results in the interaction potential $U_{\text{int}} \approx eE_\perp\xi$.

4.3.3 Current Studies

Even though the simple theoretical approaches show an increase in SSE mobility by Rydberg excitation, the effect is not fully understood yet. Measurements at low temperatures show an increase in electron mobility [16], while measurements at higher temperatures show a decrease [17][18]. The decrease can be explained by a substantial heating of the electron system through Rydberg excitation. While the excitation of electrons through MW-photons is connected with a negligible change of momentum, the relaxation through electron-vapor and electron-ripplon scattering leads to a small change in energy, but a huge change in momentum (analogous to electron-photon and electron-phonon interaction in solids). Thus, the absorbed energy is transferred to kinetic energy of the electron motion along the surface. Then, electron-electron collisions with a very high rate quickly redistribute the kinetic energy forming an equilibrium distribution with $T_e > T$ [16][18]. Even for small excitation a significant heating of the electron system occurs. To incorporate the thermal occupation of high excited subbands (n>2), it is assumed that the electrons are distributed according to the Boltzmann equation $n_n \propto \exp(-\Delta_n/T_e)$[18]. Due to the occupation of high exited states at higher T_e the number of possible states to be scattered in for intersubband scattering by vapor atoms increases (compare to density of states in solids). On the other hand the matrix element between different states decreases for higher states due to increased distance to the surface. The outcome of the increase (due to higher number of states) and decrease (due to smaller matrix element) depends strongly on the holding field [17] and therefore the distance to the surface.

4.4 Wigner-Crystallization and Bragg-Cherenkov-Scattering

Eugene Wigner predicted 1934 [19] that a 2D or 3D electron gas in uniform background will crystallize into a close-packed lattice, if the density is low enough. The localization at the lattice

sites happens when the potential energy between electrons U_{ee} becomes much larger than the (thermal) kinetic energy K_e. To describe the ratio of the mean interaction energy to the mean kinetic energy the dimensionless plasma parameter $\Gamma = \langle U_{ee}\rangle/\langle K_e\rangle$ is introduced. For the 2D electron gas the mean potential energy is $\langle U_{ee}\rangle = e^2\sqrt{\pi n_s}$ and $\langle K_e\rangle = k_bT$ as usual. Therefore, $\Gamma = e^2\sqrt{\pi n_s}/k_bT$. The transition is expected to occur for $\Gamma \geqq 130$. Theoretically the melting and hence the formation of the Wigner crystal can be described by the KTHNY (Kosterlitz-Thouless-Halperin- Nelson-Young) theory [20][21][22]. The melting occurs in two stages through continuous phase transitions from solid to hexatic to liquid. The first experimental observation of the crystallization was realized by Grimes and Adams [23] with electrons on the surface of liquid helium.

Due to the interaction with ripplons localized electrons form plasmonic states creating a surface dimple. Therefore, the formation of an electron lattice also leads to a dimple lattice. At low frequencies/ driving fields the effect of the dimple lattice on the electron lattice can be understood qualitatively in an effective mass treatment. The dimple lattice follows the movement of the electron lattice leading to a bigger effective mass $m_{eff} = m_e + m_{\text{dimple}} \gg m_e$. Therefore, the conductivity is expected to decrease compared to the liquid state.

At higher frequencies Bragg-Cherenkov scattering appears. The ripplons generated by interaction of the moving electrons and hence moving dimples can interfere constructively when the wave vector $\vec{q}$ is equal to the reciprocal lattice vector $\vec{G}$, similar to Bragg scattering. This enhancement in amplitude of the ripplons increases the scattering rate leading to an increase in momentum loss [24]. The Bragg-Cherenkov scattering results in a frequency/ driving field independent conductivity plateau. For high driving fields the sliding of the electron lattice decouples from the movement of the dimple and the Wigner crystal mobility jumps abruptly[10].

5 Experimental Methods

Confining electrons in microchannels allows for precise control of the electron system by imposed electric potential. There, interesting transport and phase transition properties like clocked electron transport [25], discrete transport through a point-contact constriction [26] [27], suppressed and re-entrant melting of a quasi-1D electron crystal [28][29][30], stick-slip motion of a Wigner solid [31] and inhomogeneous Wigner solid [32] can be observed. Motivated by that we designed and fabricated a microchannel device as well as a suited sample cell, to test the influence of microwave excitation of electrons to Rydberg states onto the conductivity of the electrons in this confined geometry. The device consists of a long central microchannel connected to two symmetrical reservoirs at its ends. Transport properties of SSEs are measured by a standard capacitive (Sommer-Tanner) method and analyzed using a lumped circuit model.

5.1 Device Structure

To study electrons on liquid helium the general structure is like a Metal-Oxid-Semiconductor Field Effect Transistor (MOSFET), in form of thin films or micro channels. The device consists of a source (left reservoir) connected to the drain (right reservoir) by an central channel, compare figure 5.1. In our device the guard electrode on the top layer is separated into 3 parts, above the left reservoir, right reservoir and central channel to allow for more precise control of the electron density n_s and holding field $E_\perp$ in the central channel. Analogous to the quasi Fermi potential in the MOSFET one can define the electron potential in the reservoirs to determine the electron density in the central channel. The depth $d = 4\,\mu m$ and width $W = 20\,\mu m$ of the channel is determined by the simulations carried out in chapter 6.

5.2 Sample Preparation

In this section first the choice of the photoresist for the isolating layer and parameters for UV-lithography will be explained. Also the determination of the etching time is explained. The procedure for the bottom and top electrode is analogous to the one in [8] and will therefore not be explained in further detail. In the last part the final manufacturing process from the wafer to the finished sample is explained.

5.2.1 Photoresist for Insolating Layer

Starting from the positive photoresist MICROPOSIT S1813 PHOTORESIST from Shipley Company, used in previous samples with the following recipe for spin coating 1. 500 RPM 10s 2. 3000 RPM 50s and a corresponding film thickness of 1.5 µm. In positive photoresist the exposed part

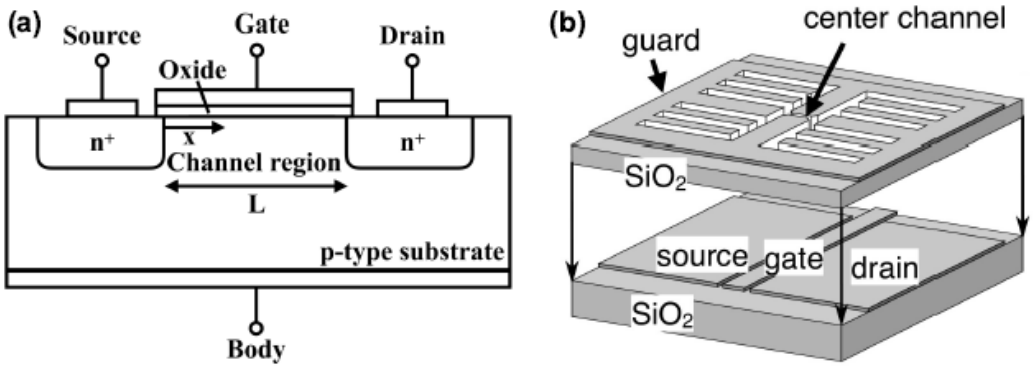

Figure 5.1: Schematic view of an microchannel device:(a) Cross section of a n-type Metal-Oxid-Semiconductor Field Effect Transistor (MOSFET). The electron density in the channel region is controlled by the voltage applied on the Gate. The current flows between source and drain. (b) Schematic picture of a microchannel device. The device consists of the top and bottom metal electrodes separated by an insulating layer. The reservoirs are connected by a central channel. The negatively-biased top- guard electrode V_{gu} confines the electrons above the center area of the channels. The electron density in the central channel is controlled by the voltages applied to the bottom gate electrode V_{ga} and Vgu. The figure is reproduced and modified from [33].

rotation speed	5000 RPM	6000 RPM	7000RPM
thickness	5.30(10) µm	4.76(10) µm	4.38(10) µm

Table 5.1: Thickness of ARN 4450-10 dependent on rotation speed

is removed during the development, while in negative the unexposed parts are removed. I modified the rotation speed to increase the film thickness. According to the data sheet a spin rate of 600 RPM should lead to the desired thickness of 4 µm. However, the slow rotation speed leads a nonuniform thickness with a increase of thickness towards the outside. Therefore, this photoresist is not suited and the negative photoresist ARN 4450-10 from ALLRESIST is used. The spatial resolution is with 3.5 µm worse than the one of S1813 with 0.2 µm. As only the bond pads for the top layer are written in this layer, this is not a problem.

For a rotation speed between 5000 and 7000 RPM the expected thickness is in the range of 4 µm. To confirm the values given in the data sheet the thickness is checked for the following recipe 1. slope 5s 2. 500 RPM 5s 3. slope 5s 4. 5000 RPM 85s, as well as 6000 RPM and 7000 RPM. Afterwards the photoresist is soft baked at 90 °C for 10 min. According to the data sheet a dose of around 90 mJ cm^{-2} is sufficient, but previous work with this photoresist showed that a dose of 3000 mJ cm^{-2} is needed. To find the right dose, the dose for different areas of the sample is set to 80, 90, 100, 2750, 3000 and 3250 mJ cm^{-2}. After exposure the samples are post baked for 10 min at 100 °C. Then they are developed in a 2.38% tetramethylammonium hydroxide solution (TMAH) for 1 min 20 s. The photoresist in the areas of the low exposure is gone after development, while the patterns for the high exposure dose are good. Under the microscope no difference between 2750, 3000 and 3250 mJ cm^{-2} is visible, therefore 3000 mJ cm^{-2} is chosen for the next steps. The sample is now hard baked at 250 °C for 30 min to increase the chemical stability for the next steps.

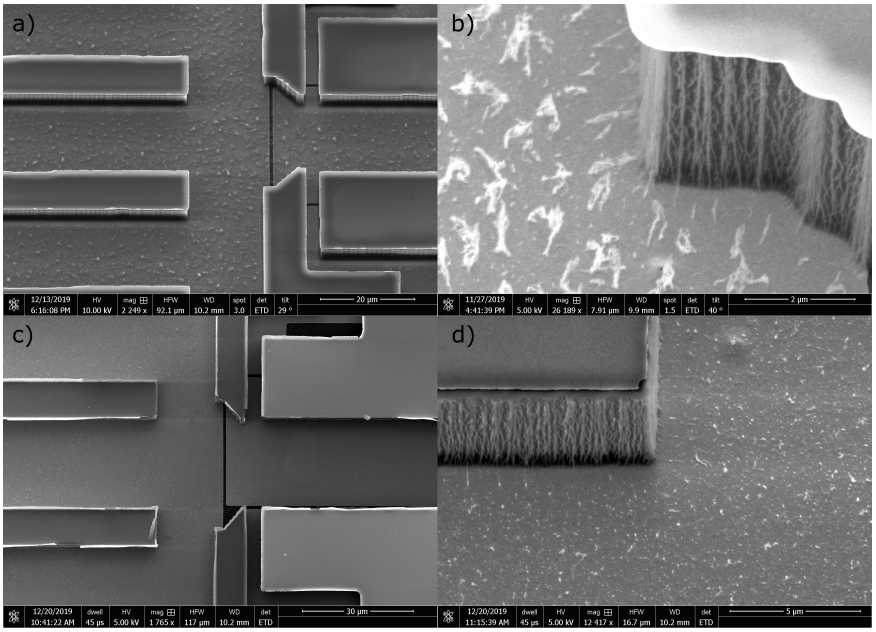

Figure 5.2: Electron microscope image of 30 and 35 min etching time: a) b) 30 minutes etching time. Big residues are visible and the surface of the bottome electrode is not smooth. The channel walls is sharp and vertical without any underetching. c) d) 35 minutes etching time. The surface looks quite smooth, but still are small parts remaining. These small residues can according to previous attempts not be removed. For both etching times is the top electrode really flat and uniform, except some damage at the edges.

The thickness for the different rotation speeds after hardbaking are shown in table 5.1. The uncertainties are determined by measurements at different sites of the sample. All values are bigger then the ones stated in the data sheet. For 7000 RPM the value is with 4.38(10) µm closest to the 4 µm determined in the simulations. As deeper channels decrease the holding field the thickness is found to be sufficient.

To test the chemical stability for development and lift off the hard-baked photoresist the sample with the rotation speed 6000 RPM is put into acetone for 21 h and measured again. Under the microscope no damage is visible, but interestingly a thickness increase from 4.76(10) µm to 5.10(10) µm is observed. The thickness of the other samples that where kept at normal air did not change. Retesting the sample with 6000 RPM 24 h after taking it out of the acetone showed a decrease to 4.90(10) µm. The hard baked photoresist seems to soak to acetone and release it after some time without getting damaged by it. As the hard-baked photo resist is not damaged by this phenomena it is not investigated further.

5.2.2 Etching Time

After depositing the top layer the channels are etched into the photoresist. To obtain sharp and vertical channel walls, highly anisotropic plasma etching is used. The top electrode is used in this case as mask for the etching. The etching rate for oxygen plasma is according to the data sheet 122 nm min^{-1}. For a thickness of 4.38(10) µm leads this etching rate to an etching time of 36 min. To avoid underetching of the channel walls, first an etching time of 30 min is tested with the following parameter of the oxygen plasma: RF power 50 W, ICP coil 100 W, DC Bias 219 V,

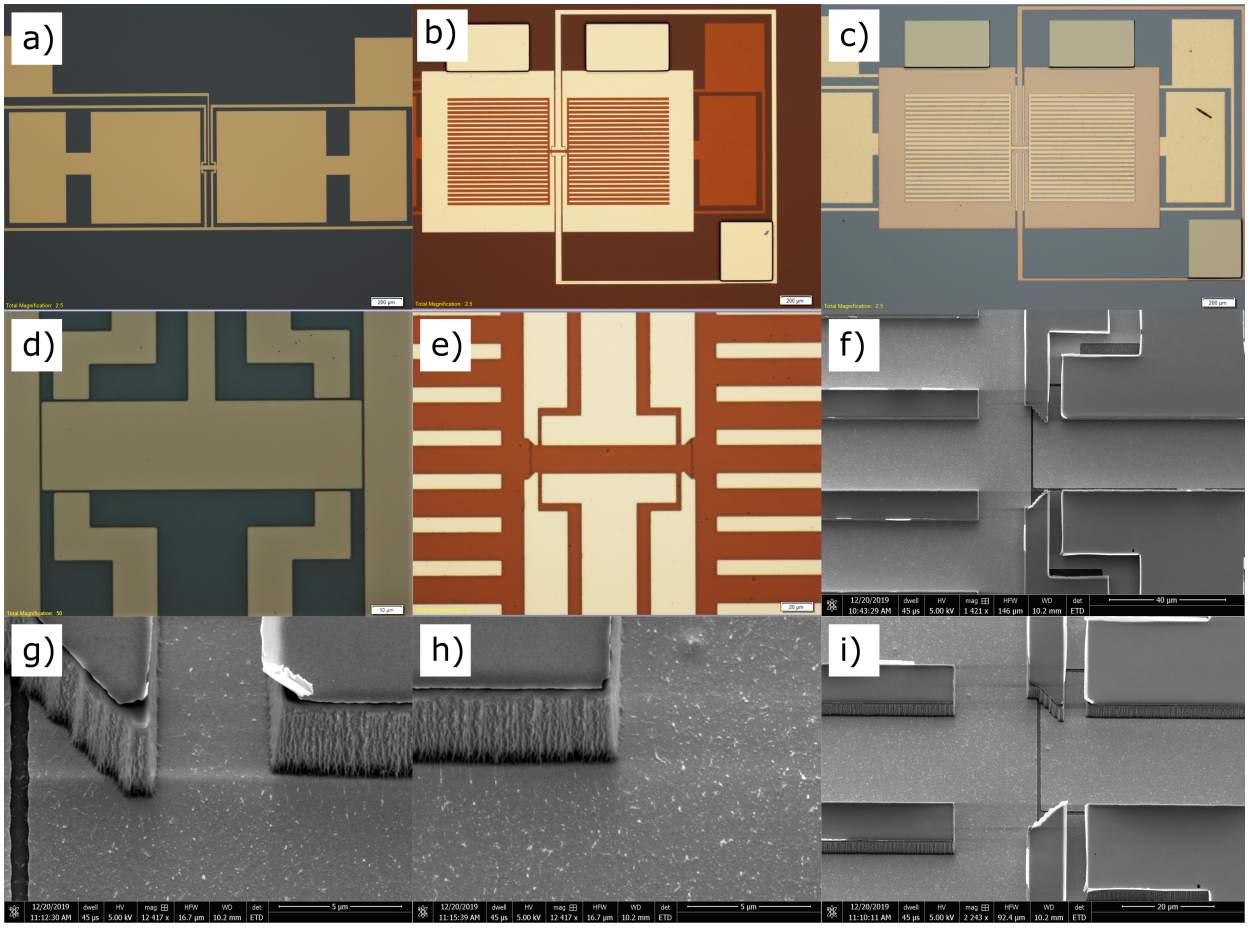

Figure 5.3: Images of the microchannel device at different preparation stages: a), d) (microscopic image) Top view after bottom layer lift off. b), e) (microscopic image) Top view after lift- off of top-layer. The bottom layer is covered by photoresist, which makes it appear darker. c) (microscopic image) Sample after etching. The bottom layer is now brighter than the top layer because of lower smoothness resulting in stronger scattering. f) (electron microscope image) Top view of the central channel. There are some bright areas along the channel edges, which indicates a rough surface. g), h), i) (electron microscope image) Images taken under a 30°-angle. The walls are vertical and straight. Especially in g) the flipped up gold from the lift off is visible. Attempts to remove this lead to the destruction of some areas of the top electrode. Also, some residues are visible, which can not be removed by increasing the etching time.

O_2 flow 10 sccm and pressure 10 mTorr. Under a normal microscope with a magnification of 100 times, no residues are visible in the channel. To verify this, the sample is checked in a scanning electron microscope (SEM) (figure 5.2 a) b)). With the increased resolution many big residue parts are visible, while some parts of the surface are clean. The top layer is flat and uniform. Also no underetching at the channel walls is visible.

Therefore, the etching time is increased to 35 min (figure 5.2 c) d)). The residues are much smaller now. For a smaller magnification is the surface of the bottom electrode flat and uniform, as well was the top electrode. The channel walls are still sharp and vertical. According to studies carried out in the group before, does a further increase in etching time not reduce the size of the residues. Additionally the underetching gets more likely with increased etching time.

5.2.3 Manufacturing Process

As pointed out above, the microchannel device is composed of bottom and top electrodes separated by an insulating layer. The bottom electrodes are the left and right reservoir, which are the source and drain in a MOSFET, a channel functioning as the gate in the MOSFET, and outer guard, which traps the electrons on the sample. The top electrode consists of the guard structures on the left and right reservoir and the split gate. The width of the channels in the central micro channel as well as on the reservoirs is 20 µm. The patterns for all layers are written by UV-lithographie.
The substrate used is a silicon wafer with 50 nm thick thermally oxidized film. Before spin coating the photoresist OFPR the substrate is cleaned for 10 min in acetone in the sonicator and 10 min in isopropanol also in the sonicator. The OFPR is spin coated with 1. 500 RPM 10 s 2. 4000 RPM 50 s and then soft baked at 115 °C for 90 s. The bottom structure is written with 70 mJ cm^{-2} for fine stuctures around the central channel and 95 mJ cm^{-2} for the rest. Afterwards it's developed in TMAH for 30 s. The electrodes are deposited in an electron beam evaporator. The bottom electrode consists out of 5 nm Titanium and 45 nm Gold, where the Titanium increases the adhesiveness of the gold film (Fig. 5.3 a) and d)). Than a homogeneous layer of 4.38(10) µm ARN photoresist is added by spincoating according to the recipe discussed above. To allow for wire bonding of the top layer without destroying the photoresist, the areas of the bondpads for the top electrodes are removed. Afterwards the insulating layer is hardbaked at 250 °C for 30 min. The top layer is prepared the same way as the bottom layer (Fig. 5.3 b) and e)). Afterwards the sample is treated with reactive ion etching (RIE) using oxygen for 35 minutes to remove the insulating hard baked (Fig. 5.3 c), f)). The top layer of gold acts as an mask for etching, which allows for vertical, sharp channel walls, as the RIE is highly anisotropic (Fig. 5.3 g), h) and i)). Finally the samples are glued to a Printed Circuit Board (PCB) (figure 5.4 a)) or an 8-lead side braze (figure 5.4 b)) and connected by a wire bonder.

5.3 Experimental Setup

In the following section, starting from the sample cell and PCB designed for this experiment the experimental setup is explained. Also the operating principle of the ^{3}He refrigerator and ^{3}He-^{4}He dilution refrigerator is explained. Then the basic measurement set up and procedure is explained.

5.3.1 Sample Cell and PCB

The sample cell used previously to study electrons confined in microchannels has no inlet for the waveguide. Accordingly, it is not possible to detect the Rydberg-excitation with this cell. Therefore I designed a new sample cell with inlets for the waveguide, inlet for the He filling line and six electrical connectors.
The cell consists of a cell body with the microwave inlet and the filling line. To be able to use the cell in different refrigerators two cell bodies were ordered (schematics in 9.29.3). One with the inlet of the filling line on the side, the other one with the inlet of the filling line on top of the cell body. The microwave inlets are set in such a way that the sample is approximately 1 mm below the center of the waveguide leading into the cell to achieve high microwave powers on the

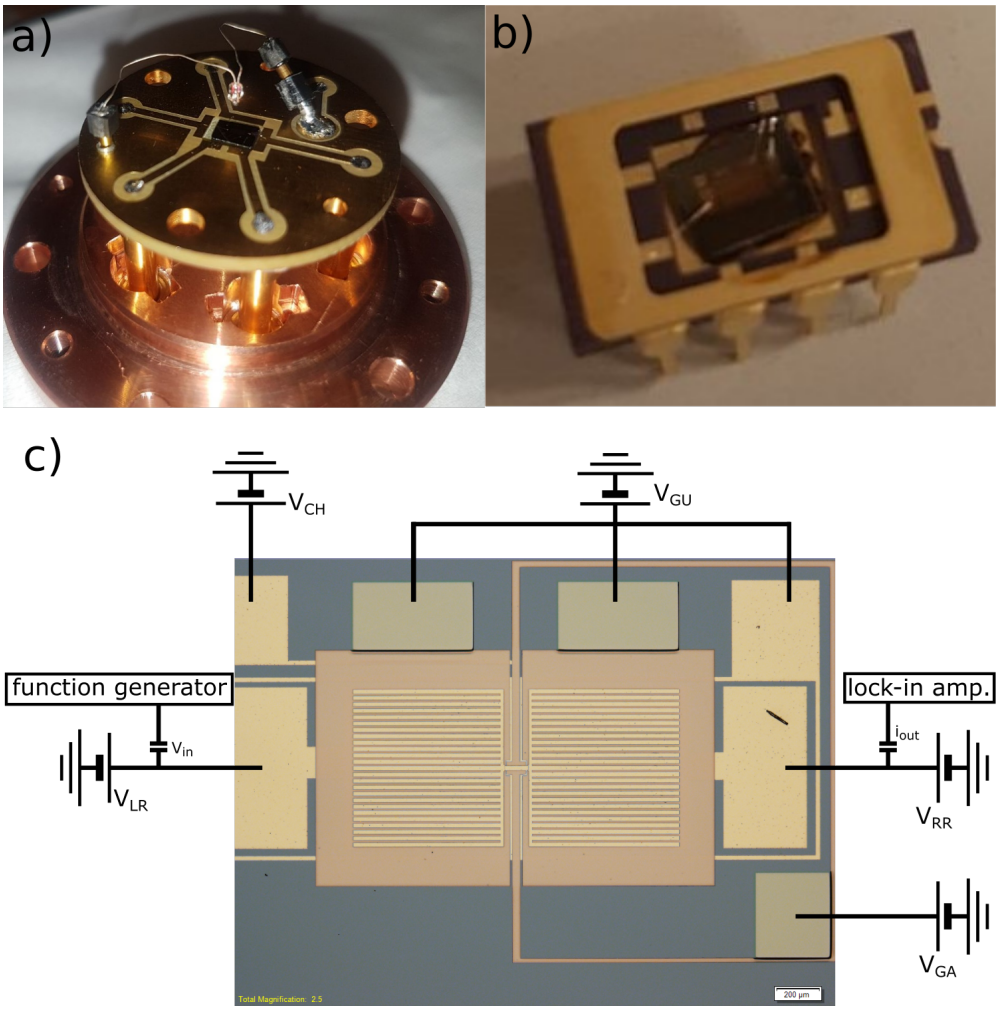

Figure 5.4: Sample mounted onto PCB and sample wiring: a) sample mounted onto the PCB with tungsten filament as electron source. The sample is connected using wire bonding. b) sample mounted onto the 8-lead side braze. c) Schematics of the potentials applied to the different electrodes. The measurement set up of the capacitive measurement with V_{in} and I_{out} is also shown.

sample. Opposite to the inlet of the microwaves is a outlet to mount a bolometer to the sample cell to absorve the microwave power in the cell. The adapters for the waveguides are sealed by kapton glued to the surface by stycast. Kapton is vacuum proof at temperatures below 100 K and transparent for microwaves.

The cell bottom is designed in a way similar to an existing one for different experiments. The schematics are in 9.1. The electric connection is done by hermetically sealed SMP male to male connectors. These are mounted into the holes designed for them, sealed by indium and then tightly screwed by a washer and nut. At the inside the SMP female to female connectors, available in various lengths, are put to set the sample 1 mm below the microwave inlet.

The sample is glued on a PCB. The design of the PCB is shown in 9.5 In the middle of the PCB is a rectangular slot reduced to a depth of 0.45 mm, around which the 5 needed bond pads for the LR, RR, CH, GA and GU electrodes are placed. On the round spot connected to the sixth connector is a adapter for one leg of the filament, a cut-open light bulb, soldered, while the adapter for the other leg is soldered to one of through holes, which is grounded. The filament is then placed in such a way that it is approximately 5 mm above the sample. It is used to charge the He surface. To mount the PCB onto the cell body and connect it electrically SMP male connectors are soldered through the holes connected with the electrodes.

For test measurements of the samples without microwaves an existing sample cell is used for the 8 lead side braze. After putting the sample the cell bottom and cell body are sealed by Indium and mounted in either a ^{3}He or a ^{3}He-^{4}He dilution dry refrigerator. At 0.8 K the cell is filled with liquid ^{4}He.

5.3.2 ^{3}He refrigerator and ^{3}He-^{4}He dilution refrigerator

The ^{3}He as well as ^{3}He - ^{4}He dilution refrigerator are both dry refrigerators. Therefore a pulse-tube is used to cool one plate, the 4 K-plate, down to 4 K, normally provided by a liquid ^{4}He bath.

In the ^{3}He refrigerator is additionally to the ^{3}He circulation line also a ^{4}He circulation line. The working principle of both cooling mechanism is the same. The He is liquefied at the 4 K-plate and then goes through a small tube impedance to the He pot. To decrease the temperature below the boiling point at normal pressure, one pumps at the He in the pot. If atoms of the vapor phase are pumped away, the most energetic ("hottest") atoms will leave the liquid to replace the vapor atoms. Therefore the mean energy decreases and the system cools down. With ^3He and ^4He one can reach temperatures of 0.3 K and 1.3 K, respectively. Accordingly, the ^{4}He circulation is used to cool down the second stage and ^{3}He for the final stage. In the experimental set up used temperatures of 0.8 K continuously or 0.6 K with a turbo pump for approximately 50 min can be reached.

In the ^{3}He-^{4}He dilution refrigerator a mixture of ^{3}He and ^{4}He is used. At temperatures below 0.867 K the mixture of liquid ^{3}He and ^{4}He separates into 2 phases, one ^{4}He rich and the other ^{3}He rich. If the temperature approaches 0 K the ^{3}He rich phase becomes pure ^{3}He, while the concentration of ^{3}He in the ^{4}He rich phase reaches a constant concentration of 6.6%. As the enthalpy of ^{3}He in the ^{4}He rich phase is larger than in the ^{3}He rich phase energy is required to

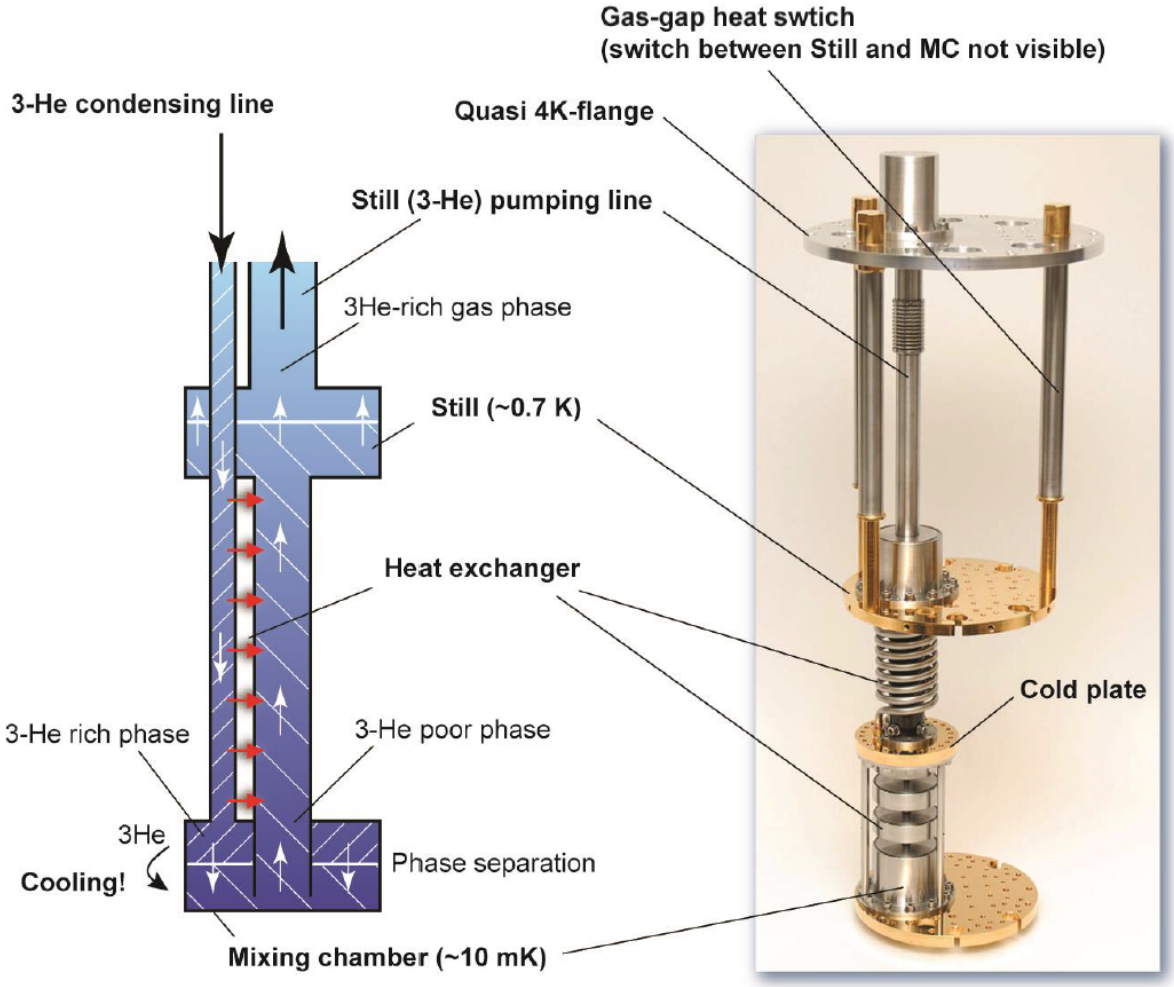

Figure 5.5: Schematics of the still and mixing chamber of the dilution refrigerator: The schematics show the flow of the liquid Helium in the dilution refrigerator. Also the names of all important parts are shown. The graphic is taken from [34]

move ^{3}He atoms from the ^{3}He rich phase to the ^{4}He rich phase. This energy is taken from the environment, so cooling occurs.

The schematics of the dilution refrigerator are shown in figure 5.5. At the start of the cooling down pumping the still will reduce the temperature due to evaporative cooling below 0.8 K. Hence the phase separation will occur and the heavier ^{4}He rich phase sinks to the bottom of the mixing chamber. Due to the higher vapor pressure of the ^{3}He than ^{4}He, mainly ^{3}He is pumped out in this state. This ^{3}He is returned to the mixing chamber. There it is forced through the phase boundary resulting in cooling. An osmotic pressure due to the pumping lack of ^{3}He in the still drives the ^{3}He from the mixing chamber to the still. [34]

5.3.3 Measurement Setup

In figure 5.4 the wiring of the sample is shown. During an experiment the channel voltage V_{CH}, gate voltage V_{GA}, left, right reservoir voltage V_{LR}, V_{RR} and the guard voltage V_{GU} can be controlled independently. To the left reservoir is additionally to the fixed voltage V_{LR} a small AC-Voltage

with frequency f and amplitude $V_{\text{in}} \ll V_{\text{LR}}$ applied. Due to the capacitive coupling of the right and left reservoir an AC current I_{out} at the right reservoir is induced. This current is amplified by a preamplifier, also providing the right reservoir voltage V_{RR} and afterwards detected using a lock-in amplifier.
SSE also couple capacitively to the reservoirs. This leads to an increased current as electrons are deposited onto the surface. The resistance of the electrons in the reservoirs can be neglected and is therefore determined by the resistance of the electrons in the central channel. There the electron density can be controlled by the channel and gate voltage V_{CH} and V_{GA}. As the helium level in the sample cell can't be detected the sample cell is filled in steps. Therefore, a He tank with a pressure gauge is used. As helium condenses inside the sample cell, the pressure in the tank decreases. The pressure decrease compared to the starting pressure of this tank is in the following chapters referred to as filling level in mbar. Generally a sample cell is filled twice. First the level is scanned to find the filling level with the highest electron current. Then the cell is warmed up and the He removed to fill it up to this ideal level. There the measurements are done.
In the dilution refrigerator a overmode waveguide for the microwaves is installed. It is connected with one end to the microwave source, with the other to the sample cell. At the opposite side of the sample cell a bolometer is mounted to detect the incoming microwaves.

6 Electrostatic Simulations

To estimate the electron density in the central micro channel and holding field, the Poisson equation is solved by finite-element modeling (FEM) in Comsol Multiphysics. The postprocessing of the data is done in Matlab connected to Comsol Multiphysics using Comsol Livelink with Matlab. The design of the samples is dictated by the limited excitation frequency of approximately 400 GHz, corresponding to a holding field of $1000\,\mathrm{V\,cm^{-1}}$. Therefore, the channel depth and width is modified, while the influence of the depression of the He film in the middle of the channel is checked.

6.1 Geometry and Model

Due to the symmetry along the central channel and the large ratio between length and width of 5 are we expecting that changes in electron density at the end of the channel - where it is connected to the reservoir, can be neglected. Therefore, we solve the Poisson equation only in a 2D-cut layer. A schematic picture of the geometry can be seen in figure 6.1 a). On the left and right side the isolating channel walls (purple) out of photoresist are visible. On top of this the split gate electrode (yellow) made out of gold can be seen. The channel electrode (yellow) extends over the whole channel, but also out below the channel wall. The channel is filled with superfluid HE due to cappilary forces. Above the gates the Helium film is very thin $\propto 1/\sqrt[3]{H}$ with height H of the structure above the helium surface. Therefore, this film is not considered in the simulations. The helium level in the center of the channel is reduced due to the pressure exerted by the electrons on the one hand and the surface tension on the other. This depression of the He in the channel ϱ can be calculated with

$$\varrho = \frac{\left(\rho g H + n_s^2 e^2 / \left(2\epsilon_{\mathrm{He}}\epsilon_0\right)\right) W^2}{8\alpha_t}\,, \tag{6.1}$$

where gravitational acceleration $g = 9.81\,\mathrm{m\,s^{-2}}$, density of liquid He $\rho = 145\,\mathrm{kg\,m^{-3}}$, width of channel W and surface tension of liquid He $\alpha_t = 3.7 \times 10^{-4}\,\mathrm{N\,m^{-1}}$ [35]. To model this depression along all the surface, a radius of curvature is calculated and implemented like in [36]. In the experimental setup it is only possible to roughly estimate the height of the sample above the He level, therefore the dependence of the depression on the electron density and holding field is investigated later. Above the liquid He is vacuum -i.e., $\epsilon = 0$.
In figure 6.1 b) a simulation for a channel depth $d = 4.25\,\mu\mathrm{m}$, depression $\varrho = 0.5\,\mu\mathrm{m}$ and a channel width $w = 20\,\mu\mathrm{m}$ is shown. The black lines represent the boundaries between different materials. The applied voltages are $V_{\mathrm{CH}} = 1V$ and $V_{\mathrm{GA}} = 0V$. In the channel walls the system can be approximated as capacitor. Therefore, we expect to see a linear decrease of the electric potential

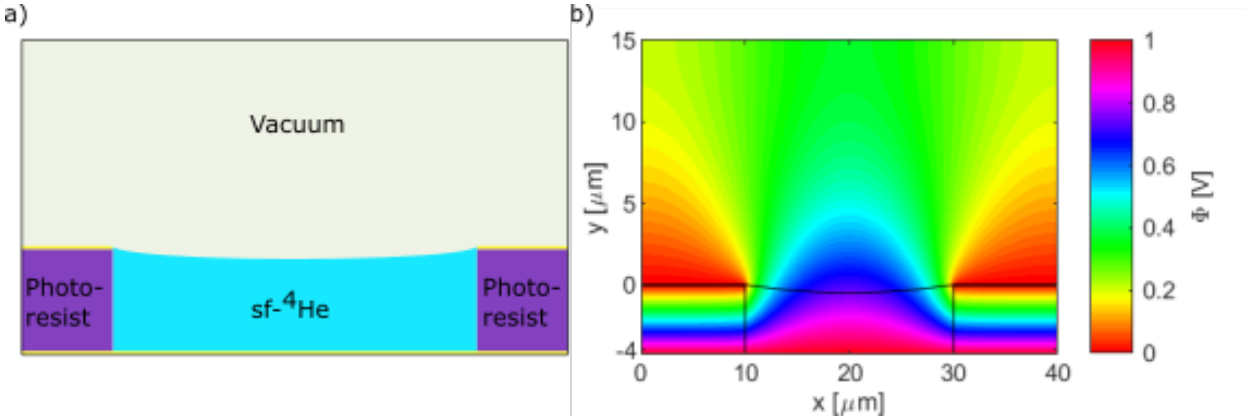

Figure 6.1: Model for FEM-simulation: In **a)** the model for the FEM-simulation is shown. The depth and width of the channel can be varied as well as the depression of the He film. The yellow rectangles resemble the electrodes. **b)** FEM-simulation for a 4.25 µm deep and 20 µm wide channel with a depression of 500 nm. The black lines resemble the interfaces between the materials shown in **a)**. One can easily see, that the potential is leaking out above the gate electrodes.

Φ with increasing height. This is visible in the simulation. At the interface between channel walls and liquid He this behavior is modified. Due to the missing compensation of the potential provided by the channel electrode the potential is leaking out above the gate electrode. There it decays slower, because the distance to the sample cell is about 8 mm and even the filament about 5 mm is at least three orders of magnitude larger than the distances in the sample. Therefore, the potential of the top boundary was set to be floating resembling the big distance between the sample and the next electrical conductors. The highest potential at the He-vacuum interface is expected in the middle of the channel and is in the following referred to as Φ_0.

To model the electron distribution across the micro channel $n_s(x)$, the electron system is treated as charge sheet with finite width w_i and potential V_e at the helium surface. This potential is determined by the voltages applied to the reservoir electrodes V_{LR}, V_{RR}, the guard electrode V_{GU} and the electron density n_s in the reservoir.

The range of V_e is limited though. If V_e is bigger (more negative) than V_{GA} the electrons are able to flow over the gate and get lost to the environment or they tunnel into the gate at some sharp points. For electron potentials V_e smaller than Φ_0 the electrons are not able to enter the center channel. Consequently, the channel is closed. Therefore, V_e can be seen in analogy to the Fermi energy in solid state physics. In a naive picture the electrons occupy states with an eigen energy smaller than $-eV_e$. Resulting from this one can think about the filling of the channel in the potential distribution shown in 6.1 b). At the interface between He and vacuum the potential $\Phi_{\mathrm{surf}}(x)$ is fixed and electrons are filled in for $\Phi_{\mathrm{surf}}(x) \geq V_e$. Therefore the effective electron width w_e as well as the electron density n_s will increase with decreasing V_e.

As the electrons in the channel couple capacitively with the channel electrodes one can write the total capacitance as $C_\Sigma = C_{\mathrm{CH}} + C_{\mathrm{GA}}$. From there the dimensionless constant $\alpha = \frac{C_{\mathrm{top}}}{C_\Sigma}$ and $\beta = \frac{C_{\mathrm{bottom}}}{C_\Sigma}$ with $\alpha + \beta = 1$. As α and β depend on the depression of the helium surface, they can be used to determine the actual depression in the channel. For an uncharged surface the potential in the middle of the channel Φ_0 can be calculated with $\Phi_0 = \alpha V_{\mathrm{top}} + \beta V_{\mathrm{bottom}}$. As pointed out

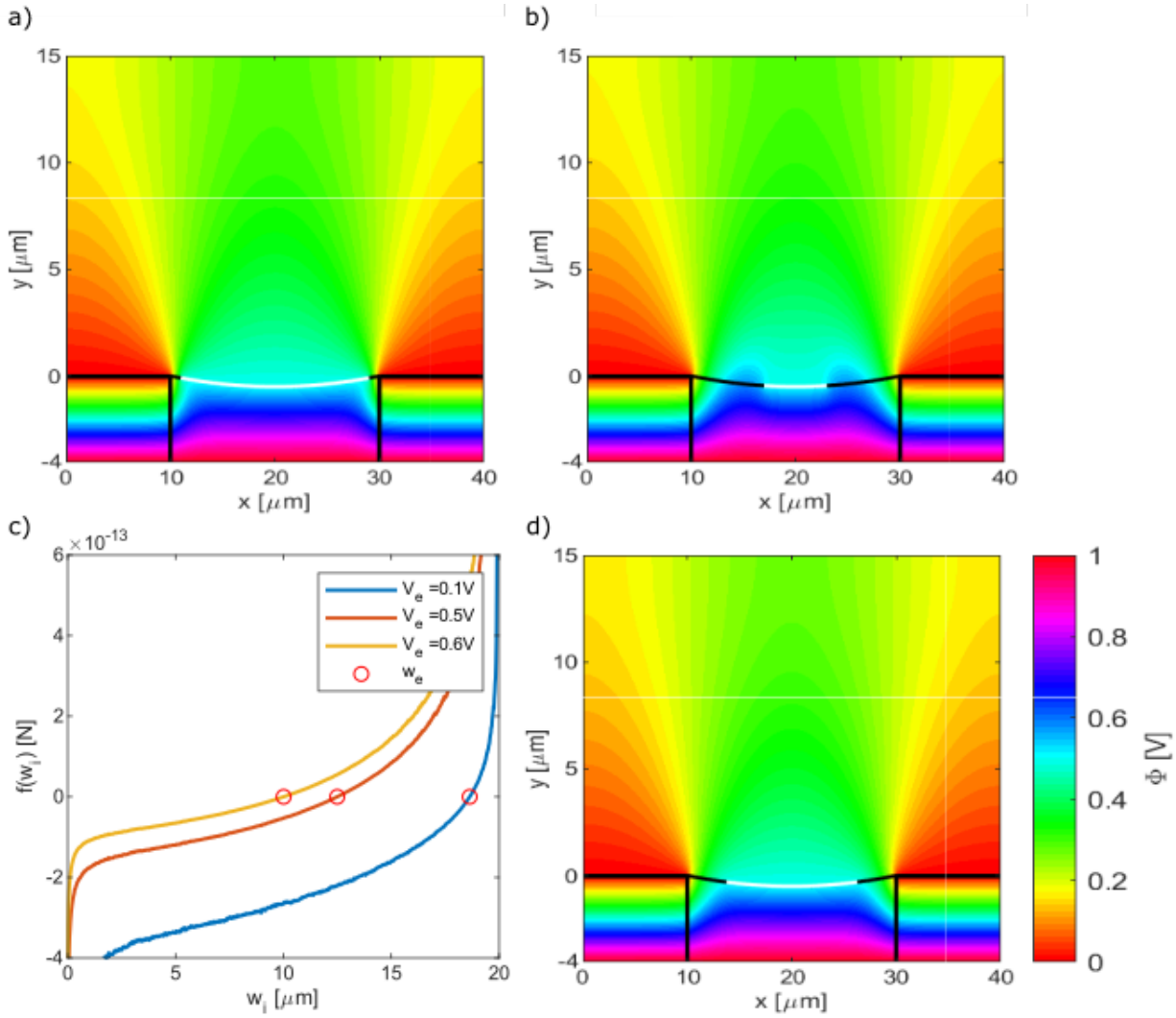

Figure 6.2: Force on the edges of the electron system: All calculations in this graphic are done for a channel width $W = 20\,\mu\text{m}$ and depth $d = 4\,\mu\text{m}$ with a depression $\varrho = 0.5\,\mu\text{m}$ and the potentials $V_{\text{CH}} = 1\,\text{V}$, $V_{\text{GA}} = 0\,\text{V}$. Additionally to the black lines resembling the boundaries between different materials the white line indicates the charge layer modeling the electron system. In **a)** and **b)** the potential distributions in the non equilibrium case with finite width $w_i = 18\,\mu\text{m}$ and $w_i = 6\,\mu\text{m}$,respectively, are shown at $V_e = 0.5\,\text{V}$. In both cases a force is acting on the edge of the electron system, but with different signs. **c)** The force acting on electrons dependent onto the finite width w_i. Each curve consists out of 1000 different w_i and appears therefore smooth. Each curve has one equilibrium position at w_e, dependent on the electron potential. The higher the electron potential V_e is, the smaller is the effective width w_e. **d)** Potential distribution for $V_e = 0.5\,\text{V}$ with the effective width $w_e = 12.25\,\mu\text{m}$.

above opens the channel at $V_e = \Phi_0$. Therefore the electron potential can be calculated using

$$V_e = \alpha V_{\mathrm{GA}} + \beta V_{\mathrm{CH,open}}\,, \tag{6.2}$$

where $V_{\mathrm{CH,open}}$ the needed channel voltage is for a fixed V_{GA}. With known α and V_e the electron density and the depression in channel can be determined.
To calculate the effective electron width w_e we numerically solve the Poisson equation with the modified potential. Then, we calculate the electrostatic force $f(w_i)$, acting on the electron system parallel to the He surface, at the boundaries of the charge sheet. If w_i is to larger then w_e (figure 6.2 a)), the electrostatic force $f(w_i)$ will push the electron system inside, while for smaller w_i (figure 6.2 b)) the electron system will be pulled outwards. Therefore, the effective electron width w_e can be found in equilibrium $f(w_e) = 0$. This is illustrated in figure 6.2. The curves are calculated with 1000 equally spaced points between $w_i = 0\,\mu\mathrm{m}$ and $w_i = 20\,\mu\mathrm{m}$. As expected each curve has one zero crossing, which marks the equilibrium position w_e. Additionally the curves are all continuous and therefore the conditions for bisection are met. This speeds up the calculation process for following simulations and allows for an accuracy down to 0.1 nm with 20 iterations of the bisection. Consequently, the error of the channel width can be neglected. In figure 6.2 d) the potential distribution Φ is shown for $V_e = 0.5\,\mathrm{V}$ with the equilibrium width w_e.
The electron density $n_s(x)$ and holding field $E_\perp(x)$ across the channel can then be calculated according to Gauß's law

$$\left.\frac{\partial\Phi(x)}{\partial y}\right|_{\mathrm{above}} - \epsilon_{\mathrm{He}}\left.\frac{\partial\Phi(x)}{\partial y}\right|_{\mathrm{below}} = -\frac{e n_s(x)}{\epsilon_0} \quad \text{and} \tag{6.3}$$

$$\left(\left.\frac{\partial\Phi(x)}{\partial y}\right|_{\mathrm{above}} + \epsilon_{\mathrm{He}}\left.\frac{\partial\Phi(x)}{\partial y}\right|_{\mathrm{below}}\right)/2 = E_\perp\,. \tag{6.4}$$

For a 20 µm wide and 4 µm deep channel with a depression of 500 nm at $V_{\mathrm{CH}} = 1\,\mathrm{V}$ and $V_{\mathrm{GA}} = 0\,\mathrm{V}$ the electron width a), average electron density b), electron density distribution across the channel c) and holding field d) are shown in figure 6.3. Even though the electron potential V_e in the experiment is fixed as stated above, it is scanned here in steps of 0.1 V. This scanning of V_e is analogous to scanning V_{CH} and V_{GA} with a fixed potential difference. As expected the channel width increases with decreasing V_e. For $V_e = V_{\mathrm{GA}}$ one expects the whole channel to be filled with electrons. The expectation is confirmed. Similar to the increase of the channel width also the mean electron density $n_{s,\mathrm{mean}}$ increases with decreasing V_e. The highest expected mean electron density in this setting is $13.5 \times 10^8\,\mathrm{cm}^{-2}$. The electrons for high V_e are concentrated to the middle of the channel. Also the density is low. For $V_e > \Phi_0$, the electron density is zero, as described above. With decreasing V_e the distribution gets wider and more uniform with a steep drop at the edges of w_e. The holding field shows an interesting behavior across the channel. In this example it ranges from $650\,\mathrm{V\,cm}^{-1}$ to $1400\,\mathrm{V\,cm}^{-1}$. For low V_e the holding field shows a maximum in the middle of the channel and then decreases fast as it approaches w_e. For high V_e, however, a minimum can be seen in the center of the channel with a small increase from there. Overall the holding field decreases with increasing V_e and corresponding decreasing electron density n_s. Therefore, at

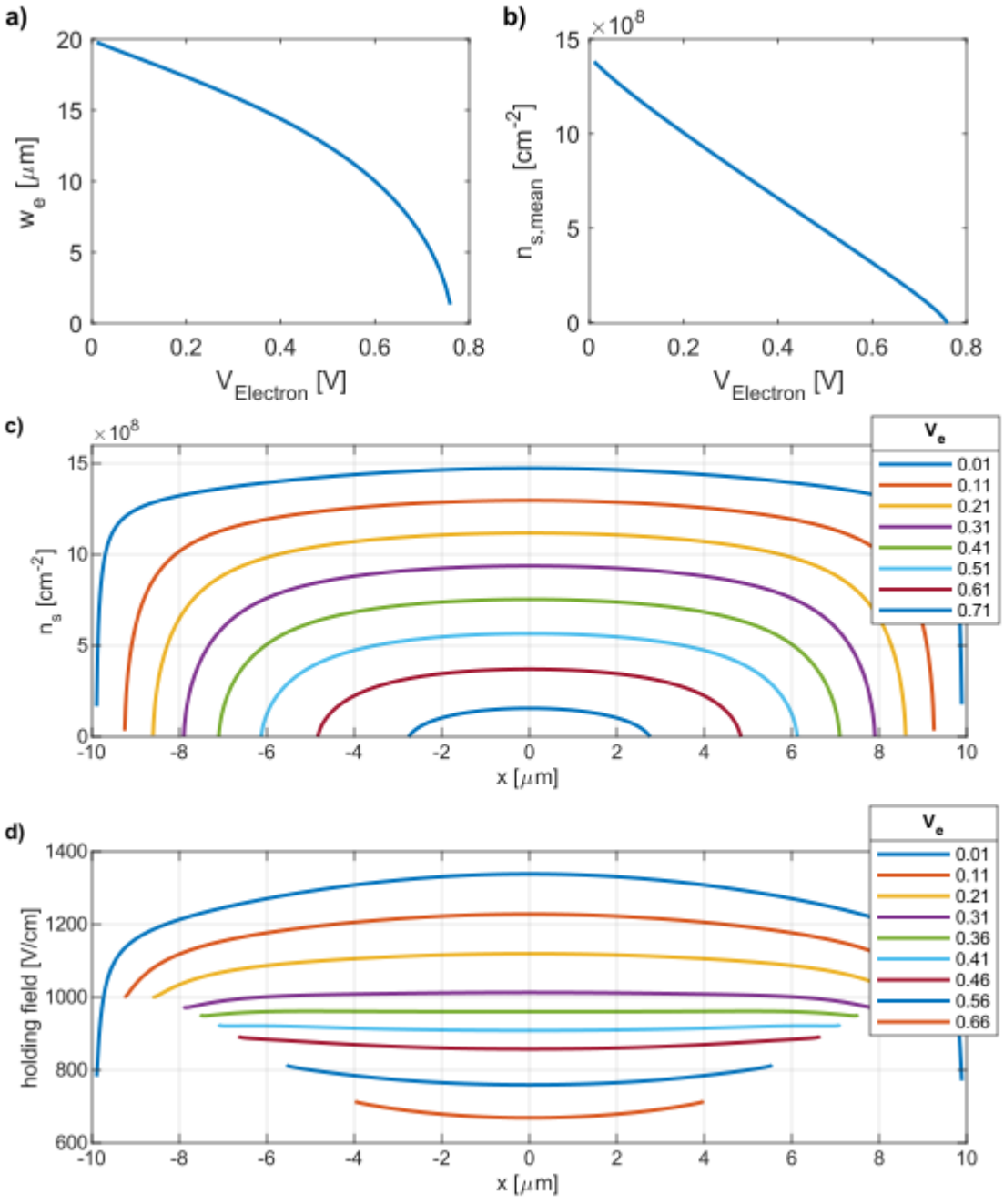

Figure 6.3: Electron density and holding field for $V_{\mathrm{CH}} = 1\,\mathrm{V}$ and $V_{\mathrm{GA}} = 0\,\mathrm{V}$: The channel simulated here is 20 µm wide and 4 µm deep with a depression of 500 nm. **a)** Effective electron width dependent on V_e. As intuitively expected the channel width increases with falling V_e. **b)** Mean electron density $n_{s,\mathrm{mean}}$ in the channel. **c)** Electron density n_s for different V_e. Especially for low V_e the density is very uniform across the whole channel. Expected densities reach up to $1.5 \times 10^9\,\mathrm{cm}^{-2}$. **d)** Holding field $E_\perp$ for different V_e. The values are only shown in the area, where electrons are present. For $V_e = 0.36\,\mathrm{V}$ $E_\perp$ is very uniform over the electron area. This results in an identical excitation frequency for all electrons in the channel.

the right V_e, here $V_e = 0.36\,\mathrm{V}$ the holding field is very homogeneous across the electron system. Due to the dependence of the excitation frequency onto the holding field this results in identical excitation frequencies for all electrons in the channel.

6.1.1 Dependence of Holding Field on Channel Depth and Width

To achieve uniform conditions for the Rydberg-excitation of all electrons, the holding field should be uniform across the channel. A non-uniform holding fields allows only for the excitation of a very limited amount of electrons. As the transition frequency depends on the holding field, only the electrons at the right position can get exited by the microwave frequency. This decreases the efficiency of the excitation and therefore higher microwave powers would be required leading to a heating of the sample cell. If the holding field is strongly dependent on the electron position, also excitation into different states with this incoming microwave frequency is possible. This reduces the comparability of the obtained data with data measured on the bulk He surface.
In the simplest model -a parallel plate capacitor with $V_e = 0\,\mathrm{V}$ at the top plate and $V = V_{\mathrm{CH}}$ at the bottom plate- the holding field $E_\perp$ at the He vacuum interface is

$$E_\perp = \frac{\epsilon_{\mathrm{He}} V}{2d}\,. \tag{6.5}$$

where d is the distance between the bottom electrode and the He-vacuum interface. Therefore, the minimal depth of the channel needed to get $E_\perp < 1000\,\mathrm{V\,cm^{-1}}$ with $V = 1\,\mathrm{V}$ is 5.28 µm.
However, in this model the depression ϱ of the He film is overlooked and also the influence of the gate electrodes is not considered. While ϱ could be considered in the calculation as a decrease of the channel depth h leading to $h \to h - \varrho$ in equation (6.5), the gate electrode cannot be considered in this way. Additionally, the channel could be only partially filled with electrons leading to a smaller compensation of the electric field than expected. To include these effects the holding field is calculated using the model developed above for various channel depths and widths, as well as various electron potentials V_e.
First the scaling behavior with fixed channel width is characterized. Therefore, two different channel widths W are chosen for evaluation: 10 µm and 20 µm. Due to the W^2 dependence of the depression it is expected to be $\varrho = 125\,\mathrm{nm}$ and $\varrho = 500\,\mathrm{nm}$, respectively.
The results are shown in figure 6.4. In a) and b) the holding fields across the channel with width $W = 10\,\mu\mathrm{m}$ for electron potentials $V_e = 0.01\,\mathrm{V}$ and $V_e = 0.25\,\mathrm{V}$ are shown. As expected the holding field decreases with increasing channel depth. Also a decrease of the holding field with increasing electron potential is visible. This decrease is due to the decrease of the potential difference. In c) and d) the average holding fields for various V_e at channel width 10 µm and 20 µm are shown. The error bar represents the standard deviation of the holding field. The red line shows the standard capacitor model of (6.5) with slope -1 in the log-log graph is in both cases parallel to the values of the FEM-simulation. But especially for the narrower channel, the holding field of the simulation is smaller. This is in conflict with the expectation of an increase in holding due to the decrease of effective distance with the depression. For the wider channel the influence of the depression is more prominent, especially for shallow channels with 1 µm. For deeper channels the value of the holding field decreases even below the one expected for a capacitor. For both channel widths

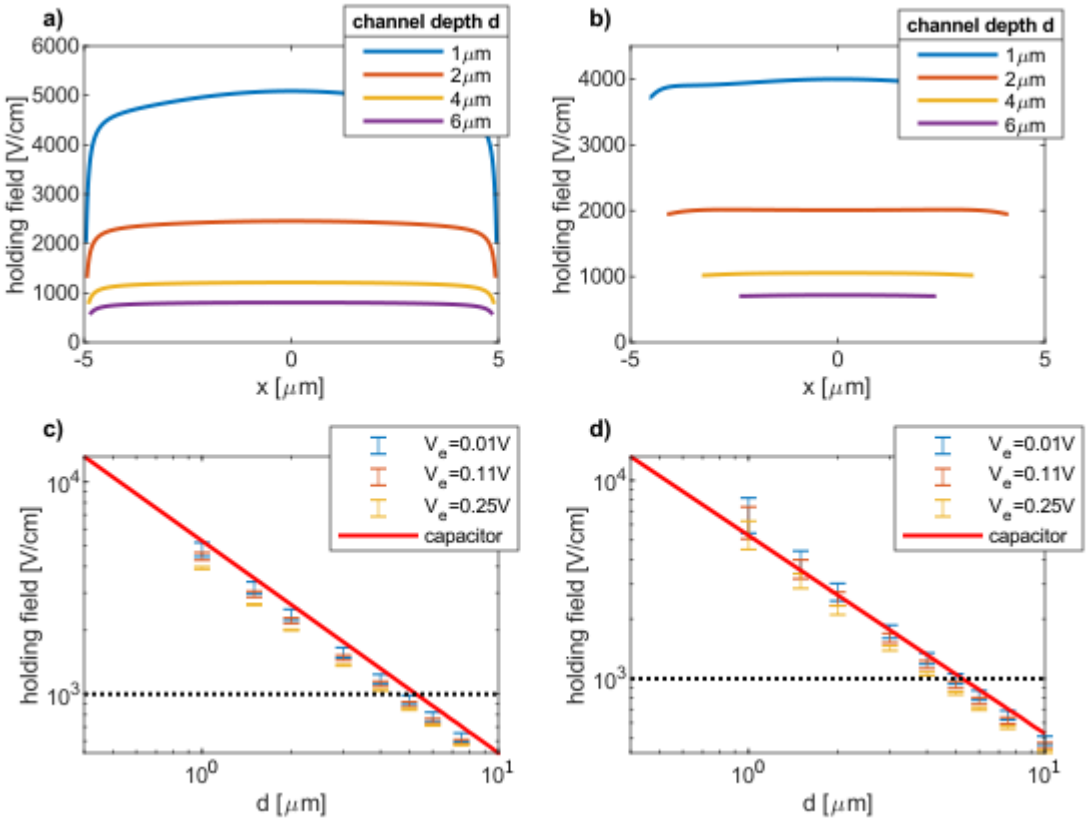

Figure 6.4: Holding Field $E_\perp$ at fixed channel width: a) Holding field for a channel width of 10 µm and a electron potential of $V_e = 0.01\,\mathrm{V}$. **b)** Holding field for a channel width of 10 µm and a electron potential of $V_e = 0.25\,\mathrm{V}$. For a deeper channel the holding field decreases as expected. Additionally the effective electron width w_e decreases as the channel depth increases. **c)** Average holding field for various channel depths at a channel width of 10 µm. The uncertainty bars resemble the standard deviation of the holding field. The red line shows the expected holding field for a parallel plate capacitor with the corresponding depth d shown in equation (6.5). The black dotted line resembles the maximum holding field in the experiment due to the maximum microwave frequency of 400 GHz. **d)** Average holding field for various channel depths at a channel width of 10 µm.

the maximum holding field of $1000\,\mathrm{V\,cm^{-1}}$, is limited by the microwave source, not exceeded for channel depths of 5 µm or more. Even for 4 µm the holding field is with $1057\,\mathrm{V\,cm^{-1}}$ close to the maximum holding field for $V_e = 0.25V$. Overall we can conclude that the scaling of the holding field in channels follows the scaling expected for a parallel-plate capacitor. However, the values simulated are, opposite to the expectation, a bit smaller than for a parallel plate capacitor.

Second, the dependence of the channel width onto the holding field is investigated. For two different channel depths, 2 µm and 4 µm, is the channel width varied. With the channel width also the depression of the helium surface is varied according to (6.1) with W^2. As reference value a depression of 500 nm at a channel width of 20 µm is taken.

The holding fields across the channels with different width and a depth of 2 µm are shown in figure 6.5 a) and b) with $V_e = 0.01\,\mathrm{V}$ and $V_e = 0.25\,\mathrm{V}$, respectively. One can immediately see the increased width of the holding field shown in the graphs with increasing channel width. This is due to the increase of the electron width w_e with the channel width. Also an increase in the holding field is visible due to the increased depression of the He film in the middle of the channel. Besides that the dependence of the holding field from the relative position in the channel is almost the same in case of a). For b) an interesting change in the shape is visible. For a width of 7.5 µm and 10 µm the holding field shows a plateau. Additionally, the average holding is smaller than at 5 µm. This is contradictory to the expected increase due to an increase of the depression in wider channels. There the leaking out of the field seems to be more prominent than the decrease of the distance to the bottom electrode. This hypothesis is supported by the formation of the plateau in the holding field. While the leaking out of the field is most prominent in the middle of the channel, it decreases towards the edges. Therefore, the holding field is decreased the most in the middle of the channel compared to the value expected in a parallel plate capacitor. While going out to the edges of the channel the leaking decreases as well as the depression leading to an increase of the field. Owing to that, the holding field stays constant over all the channel for the right electron potential depending on the depression.

In c) and d) the values for different widths are shown with a depth of 2 µm and 4 µm. While the average values for 2 µm up to a width of 20 µm are almost constant and very close to the holding fields expected in a parallel plate capacitor model , for 4 µm a decrease in holding field compared to the parallel plate capacitor model is visible. This decrease could be expected for $V_e > 0\,\mathrm{V}$, but is also prominent for $V_e = 0.01\,\mathrm{V} \approx 0\,\mathrm{V}$. In both cases the holding field increases for channel widths $W > 20\,\mu\mathrm{m}$. For $d = 2\,\mu\mathrm{m}$ the increase appears at $W = 40\,\mu\mathrm{m}$ up to $1 \times 10^5\,\mathrm{V\,cm^{-1}}$ due to the depression of 2 µm. The distance between the bottom electrode and electron charge layer vanishes and therefore the holding field goes to infinity. For 4 µm one can see the formation of the plateau described above. For $V_e = 0.01\,\mathrm{V}$ the holding field increases slightly due to the increase of the depression. However, for $V_e = 0.25\,\mathrm{V}$ the holding field decreases from the initial value to an almost constant value for increasing channel widths, up to $W = 20\,\mu\mathrm{m}$. One expects to see this effect more clearly for even higher V_e. Also in this case an increase of the holding field for $W > 20\,\mu\mathrm{m}$ above the value expected in the parallel plate capacitor model is visible. Therefore, channels wider than $W = 20\,\mu\mathrm{m}$ seem to highly increase the holding field and are consequently not practical for this experiment.

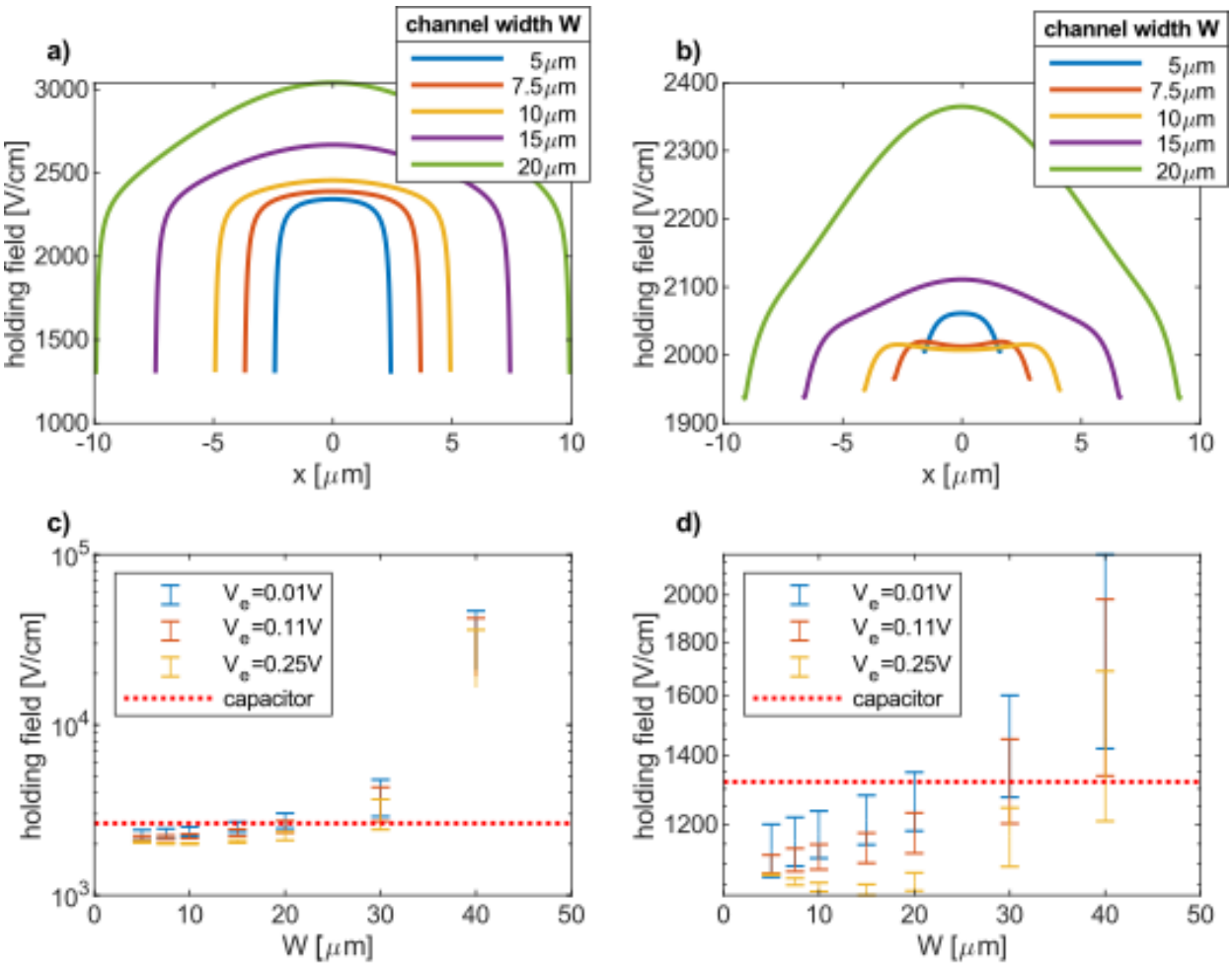

Figure 6.5: Holding Field $E_\perp$ at fixed channel depth: a) and **b)** show the holding field across the channel for a channel depth of 2 µm at $V_e = 0.01$ V and $V_e = 0.25$ V respectively. According to equation (6.1) is also the depression of the helium film varied. The width of the holding field shown varies due to the variation of the channel width. In **a)** does the overall shape not change much, while in **b)** a change and increase is visible. In **c)** and **d)** are the average holding fields for a channel depth of 2 µm and 4 µm, respectively, shown. Up to a channel width of 20 µm does the holding field not increase with increasing channel width. For a channel depth of 4 µm is the holding field even lower than expected in the parallel plate capacitor model (red line). For wider channel (>30 µm the holding field increases, especially for the shallower depth of 2 µm.

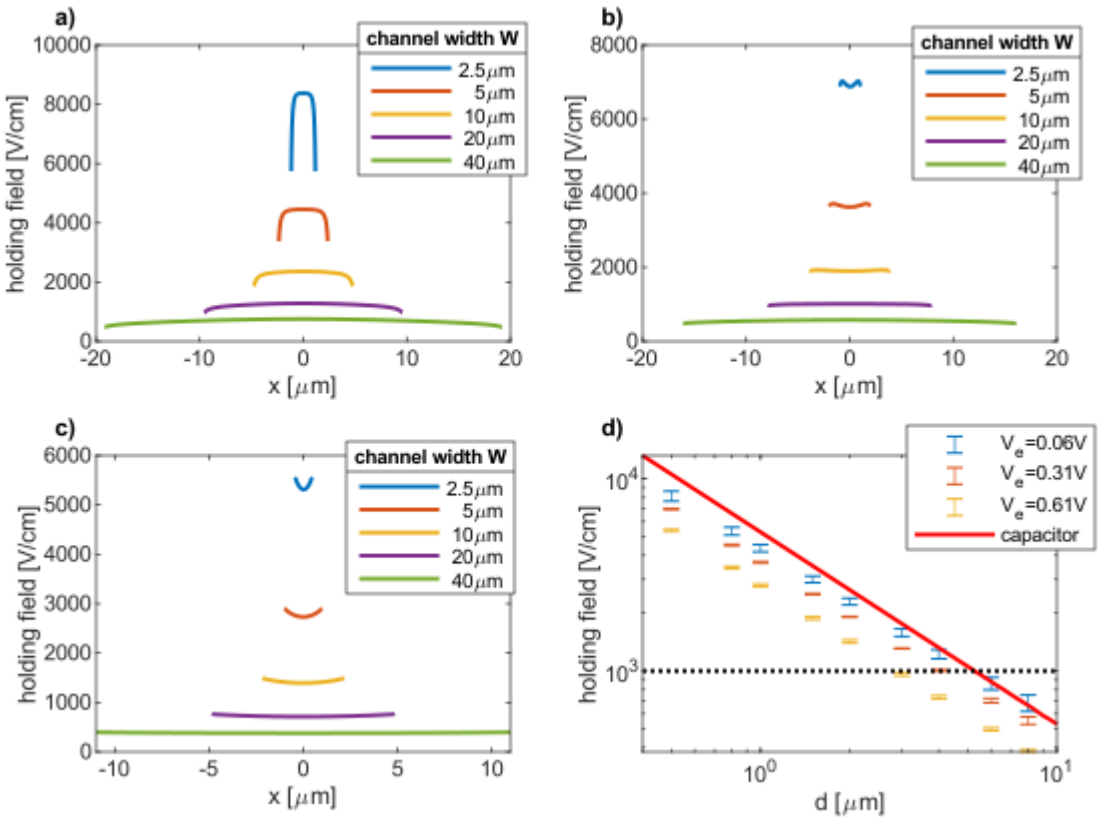

Figure 6.6: Holding Field $E_\perp$ at fixed aspect ratio of 5: In **a), b)** and **c)** is the holding field across the channel shown for $V_e = 0.06\,\mathrm{V}$, $V_e = 0.31\,\mathrm{V}$ and $V_e = 0.61\,\mathrm{V}$ respectively. The behavior is the same as shown in figure 6.3. The different length of the lines is due to the different size ranging from 2.5 µm up to 40 µm. **d)** Scaling of the holding field with the channel depth $d = W/5$. As expected is the slope similar to the parallel plate capacitor model. The black line resembles the holding field, up to which Rydberg excitation by the available microwave sources can be provided.

At last, the scaling behavior with a fixed aspect ratio W/d between channel width W and depth d is investigated. The chosen aspect ratio is 5, comparable with the aspect ratio of previous works done with micro channels [33][8][29]. As before, the depression is varied according to $\varrho \propto W^2$.
In figure 6.6 a), b) and c) the holding field distributions for $V_e = 0.06\,\mathrm{V}$, $V_e = 0.31\,\mathrm{V}$ and $V_e = 0.61\,\mathrm{V}$ are shown. While the width of the holding field is proportional to channel width, it seems that the behavior is solely correlated to the electron potential V_e. The behavior is similar to the one discussed in figure 6.3. With increasing V_e the holding field decreases. Also the transition to an almost constant holding field can be observed (b)).
In d) the holding field dependent on the depth of the channel is shown. For all voltages the values are deducted from the simulation smaller than the parallel plate model (red line). For the channel with depth 4 µm the holding field for $V_e = 0.31\,\mathrm{V}$ and $V_e = 0.61\,\mathrm{V}$ is bellow the maximal holding field of $1 \times 10^3\,\mathrm{V\,cm^{-1}}$. This is sufficient, because the distribution of the holding field over the channel is very flat in this region. For lower V_e the holding field is too inhomogeneous to achieve an excitation of a majority of electrons.
Concluding from that, we find that the channel depth of 4 µm and width of 20 µm is sufficient to get holding fields below $1000\,\mathrm{V\,cm^{-1}}$. Wider channels could lead to an increase of the holding field as observed in figure 6.5. While the holding fields in smaller channels are smaller for low V_e the decrease for higher V_e is less prominent. Also the formation of a homogeneous holding field can be suppressed due to the reduced depression of the helium film.

6.1.2 Dependence of Holding Field on Surface Depression

Due to the large width W of the channel with 20 µm and the W^2 scaling of the depression can't be neglected compared to previous works done with smaller channels like [37]. As pointed out above the depression influences the behavior and value of the holding field.
Therefore, the influence of the change in holding field with a change of depression from 0 µm to 2 µm is investigated. From a naive point of view, an increase in depression will only increase the holding field, as it decreases the distance between the electron layer and channel electrode. However, it also alters the shape over the holding field across the channel, as briefly mentioned in the previous chapter. The increase in holding field is clearly visible in the average holding fields for various electron potentials, see figure 6.7 a). Additionally to the increase of the holding field with the depression, also a increase with decreasing electron potential is visible. This has already been pointed out in the previous chapters. The increase of the holding field seems to be, besides a constant offset, only weakly dependent on the electron potential. However, the holding field distributions across the channel are more interesting.
At $V_e = 0.01\,\mathrm{V}$ the holding field is very homogeneous for small depressions (b)). This can be explained by a parallel-plate capacitor model. As the potential of the surrounding gate electrode $V_{\mathrm{GA}} = 0\,\mathrm{V}$ this forms a perfect parallel-plate capacitor with some variation in the dielectric material (He vs photoresist). As the depression is increased, the distance between the two capacitor plates decreases locally. Due to this local decrease, especially in the middle of the channel, the holding field there is increased. At the edges the influence is very small owing to the smaller depression. As the electron potential is increased the holding field decreases. Additionally the shape changes.

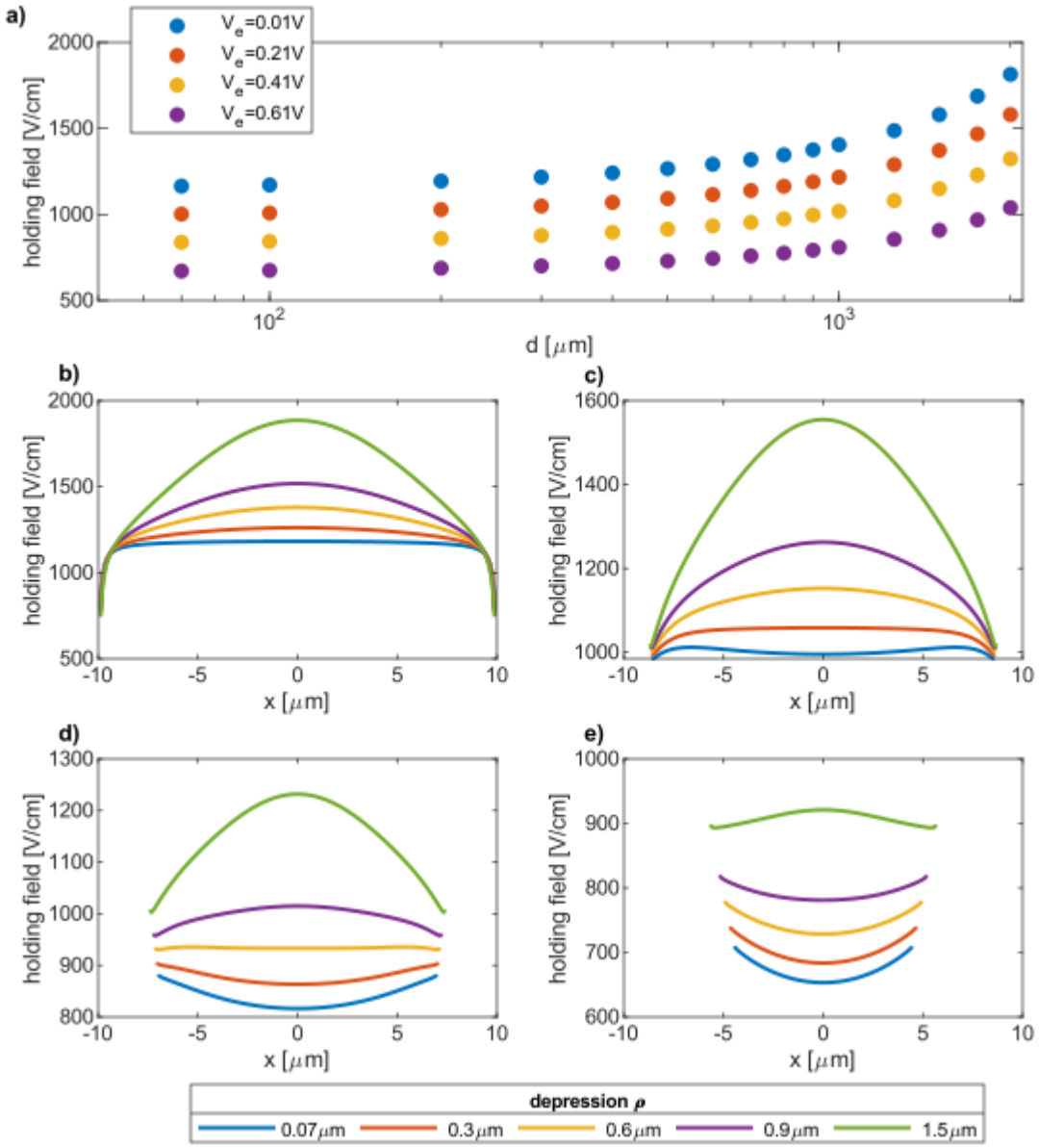

Figure 6.7: Holding field in dependence of the depression: The channel is 4 µm deep and 20 µm wide. The simulations were done for four different electron potentials **b)** $V_e = 0.01\,\mathrm{V}$, **c)** $V_e = 0.21\,\mathrm{V}$, **d)** $V_e = 0.41\,\mathrm{V}$ and **e)** $V_e = 0.61\,\mathrm{V}$. Overall we find an increase of holding field with increasing depression. This is also confirmed by the average holding fields shown in **a)**. Besides the overall increase of the holding field with the depression also the shape changes. The homogeneous holding field is therefore achieved for the right combinations of electron potential V_e and depression ϱ. Most prominent is this feature in **d)**, where both curvatures and also an almost flat line is visible.

At $V_e = 0.21\,\mathrm{V}$ the holding field is homogeneous for a depression of $0.3\,\mu\mathrm{m}$, while the holding field for $\varrho = 0.07\,\mu\mathrm{m}$ shows a local minimum in the center. Higher depressions still show a maximum in the holding field due to the reasons given above. The occurrence of the minimum is due to the decrease of the potential difference between the electron layer and the channel electrode. For an electron potential $V_e = 0.41\,\mathrm{V}$ the behavior is even more prominent. The depressions $\varrho = 0.07\,\mu\mathrm{m}$ and $\varrho = 0.3\,\mu\mathrm{m}$ show a global minimum in the middle, whilst the holding field is very homogeneous for $\varrho = 0.6\,\mu\mathrm{m}$ or even showing the opposite curvature for higher depressions. For $V_e = 0.61\,\mathrm{V}$ the homogeneous holding field is shifted to even higher depressions. Also a further decrease of the electron width is visible, as already discussed in the previous chapters.
Overall I conclude that the curvature of the holding field depends on the electron potential as well as the depression. The higher the depression the higher must also the electron potential be to achieve a homogeneous holding field.

6.2 Image Charge Detection

Besides the transport measurement to measure the change of conductivity also the image charge detection, demonstrated in [38], could be implemented. Therefore it is necessary to know the image charge imposed onto either the channel or gate electrode by the excitation of a single electron from the ground to the first excited state. Since the coupling between the electron system and the channel electrode is roughly a factor of two larger than the coupling between gate electrode and electron system, the calculations will be performed for the channel electrode.
To calculate the charge imposed by a single electron at position $\vec{r}$, the Shockley-Ramo theorem [39][40], widely applied in calculations for radiation detectors, is used. It states that the image charge induced on an electrode by a charge q at position $\vec{r}$ can be obtained by calculating the potential distribution without the charge. Therefore, all electrodes are set to be $0\,\mathrm{V}$, except the desired electrode, which is set to be $V_{\mathrm{EL}} = 1\,\mathrm{V}$. Then the image charge induced by the charge q onto the electrode can be calculated by $q_{\mathrm{image}} = q \cdot V(\vec{r})/V_{\mathrm{EL}}$. The image charge change, when a particle moves from $\vec{r}_1$ to $\vec{r}_2$, can consequently be calculated by $\delta q_{\mathrm{image}} = q/V_{\mathrm{EL}} \cdot (V(\vec{r}_2) - V(\vec{r}_1))$.

This calculation is implemented using a model similar to the one shown in 6.1 b). In the modified model, the size of the vacuum is increased and the outer boundaries are set to be $0\,\mathrm{V}$ as required by the Shockley-Ramo theorem. V_{GA} and V_{CH} are set to be $0\,\mathrm{V}$ and $1\,\mathrm{V}$. The potential is evaluated at two lines parallel to the surface at distances corresponding to the average distance of the electrons in the ground state and the first excited state with a holding field of $1000\,\mathrm{V\,cm^{-1}}$. Then the potential difference between two the excited and ground state is calculated. Next the potential difference is scaled with the electron density, to consider the non-uniform density in the channel. The total induced charge can be calculated by integration over the whole channel.
If the holding field is inhomogeneous only a small fraction of the electrons will be excited and the signal is therefore is not detectable. Consequently, the holding field must be homogeneous. For the fabricated channel with depth $4.25\,\mu\mathrm{m}$, width $20\,\mu\mathrm{m}$ and a depression of $0.5\,\mu\mathrm{m}$, the homogeneous holding field can be achieved with $V_e = 0.41\,\mathrm{V}$. For the channel length of $90\,\mu\mathrm{m}$ the charge induced onto the channel electrode is $8.3066 \times 10^{-19}\,\mathrm{C} = 5.18$ electrons for a excitation of half of

the electrons to the first excited state. In the current work an image charge change of about 20 electrons has been detected [38]. Therefore, it seems to be possible to implement the image charge detection in channels.
To increase the signal, one could try to reduce the depression. This also decreases the electron potential V_e, at which a homogeneous holding field is achieved. Therefore, the electron density in the channel increases and accordingly also the induced change of charge is increased. Additionally the channel length can be increased leading overall to a higher number of electrons in the channel.

7 Experiments and Discussion

Due to the long delivery time of the designed cell, the samples mounted on the 8 side-lead sample holder are tested in a ^{3}He-cryostate using existing vacuum-tight cells. The temperature in the normal steady state mode is 0.8 K and therefore only mentioned, if the temperature deviates from this temperature. Using a turbo pump mounted on top of the refrigerator the temperature can be reduced to 0.6 K for approximately 1 h. I do two cool-downs with two cells in each cool-down in the ^{3}He refrigerator and one with the designed cell and connected microwave guides in the dilution refrigerator.

7.1 First Cool-Down

In the first cool-down the existing cells are used for both samples. Sample 1 shows only a current pick-up, while the filament is fired. In Sample 2 a pick-up is observed, but with increasing V_{LR} & V_{RR} electrons are deposited onto the surface and stayed there.

Sample 1

The level of the helium in the cell was increased from a pressure range of 240 to 320 mbar. At every level the deposition of electrons was tested. As soon as the filament is fired the pick-up current is visible. If the voltage applied to the filament is too low, no electrons are emitted and therefore no pick-up is visible. Changing the channel, gate, guard and reservoir voltages does not change the pick-up signal. After firing the filament once, the pick-up signal of the second time firing the filament decreases, but relaxes after some time. The curve at 250 mbar is shown in figure 7.1.

7.1.1 Sample 2

For this device, the deposition of electrons is possible. Firing the filament leads to a pick-up current, as shown in figure 7.2 at a filling pressure of 240 mbar. After 200 s the $V_{\mathrm{LR}} = V_{\mathrm{RR}} = 0.3$ V is set. Now firing the filament also leads to a pick-up current, but additionally the current stays at a higher value than the background current. This shows that electrons are deposited onto the helium surface in the channels. Firing the filament a second time increases the current and consequently also the electron density in the channels, as the capacative coupling between electrons and reservoir is increased with an increased number of electrons. Further deposition of electrons does not change the current and therefore the electron density.
To characterize the behavior of the sample and determine the electron potential in the reservoirs the gate and guard voltage is scanned in finite steps. One scan at 260 mbar is shown in figure 7.3. As described in the simulation section the channel is closed, if the minimum potential Φ_0

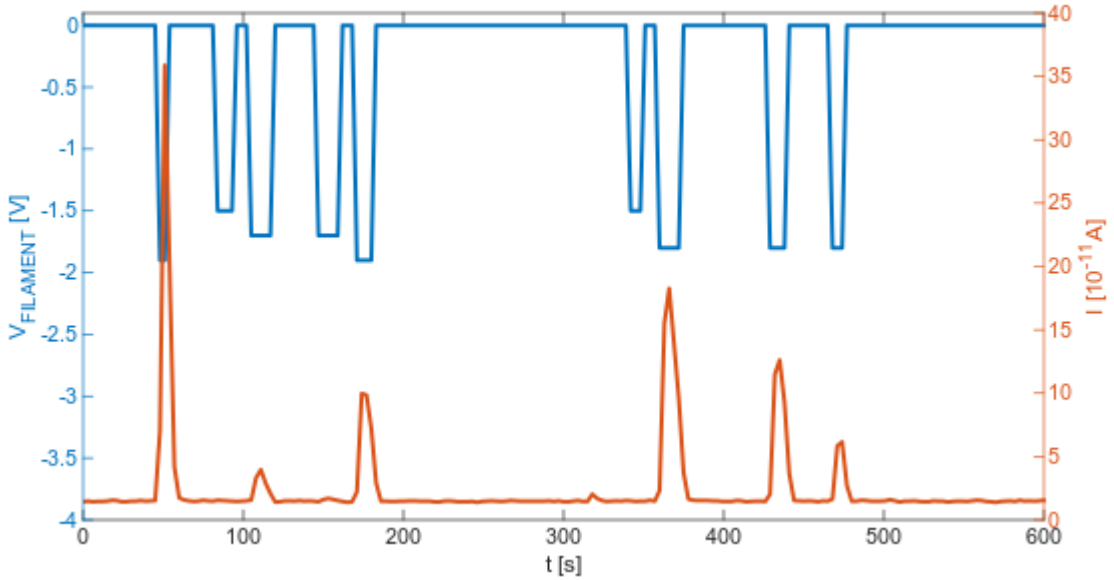

Figure 7.1: Deposition of electrons onto sample 1: The baseline is the background current due to the capacitive coupling of the two reservoirs. If the filament is fired (left axis), one can see a pick-up current (right axis). After the pick-up the current goes back down to the background current. Therefore, no electrons are bound to the surface of the Helium.

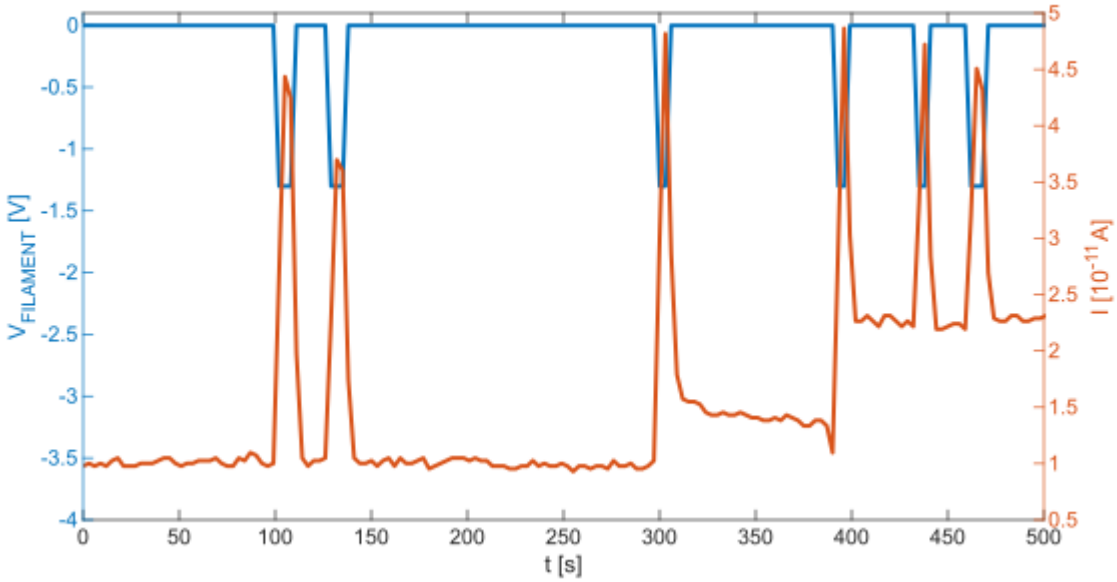

Figure 7.2: Deposition of electrons onto sample 2: For the first two peaks $V_{\mathrm{LR}} = V_{\mathrm{RR}} = 0\,\mathrm{V}$ with $V_{\mathrm{GU}} = -0.1\,\mathrm{V}$, $V_{\mathrm{CH}} = 1\,\mathrm{V}$ and $V_{\mathrm{GA}} = -0.1\,\mathrm{V}$ There is only a pick-up visible. At 200 s the $V_{\mathrm{LR}} = V_{\mathrm{RR}} = 0.3\,\mathrm{V}$. There is still a pick-up, but afterwards the current decreases to a value higher than the background, indicating that electrons are trapped in the device. A second deposition increases the current and corresponding the electron density in the device. Further depositions do not increase the current.

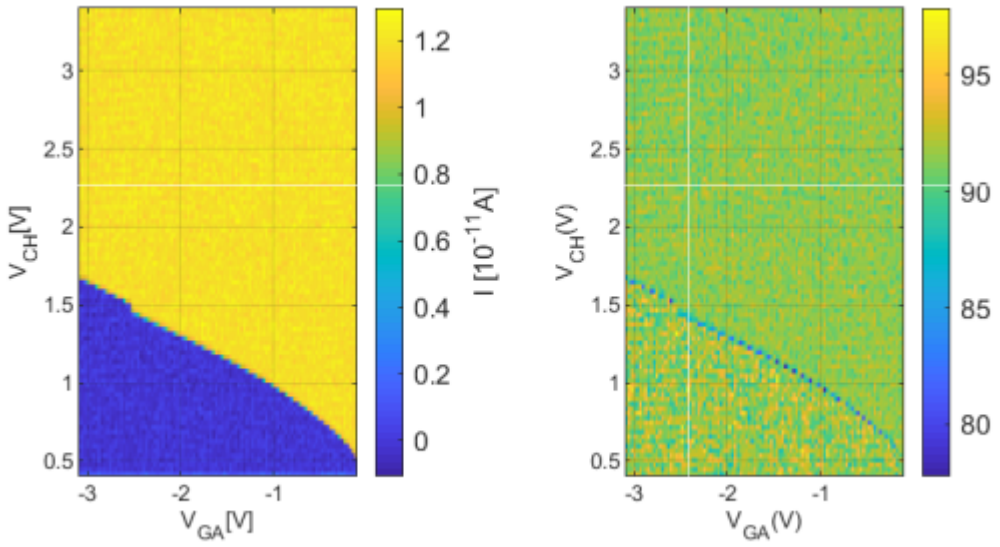

Figure 7.3: Scan of V_{GA} and V_{CH} at 260 mbar**:** The voltage V_{CH} needed to open the channel increases with decreasing V_{GA}. At the point of the channel opening the current I (left) increases up to 1.3 A. The channel opening is also visible in the phase shift (right). The electrons in the channel also lead to a more stable phase shift.

is too negative. It opens as soon as $V_e = \Phi_0$ and is showing a sudden increase in the current I. Therefore, the channel voltage V_{CH} needed to open the channel increases as the gate voltage V_{GA} is more negatively. The opening of the channel is also visible as a drop in the phase shift right at the channel opening. For the open channel the phase is more stable due to higher current. However, the phase shift shows besides the more stable value no difference between open and closed channel. As one scan with the resolution 100 steps per V_{GA} and V_{CH} takes around 8 h and no change in the current is visible, all electrons are trapped in the device for at least this time. It was not possible to achieve a break-through to the channel electrode even if the potential $V_{CH} = 10$ V was set. As the channel voltage V_{CH} is increased for a fixed gate voltage V_{GA} the electron density in the central channel also increases. One expects therefore to see the Wigner crystallization of the electrons. This is not observed in this sample. However, it is not clear if the crystallization takes place in the scanned region.

To check the sample at a lower filling level the cell is warmed up to 7 K, the helium taken out and then again filled into the cell at 0.8 K. Now the filling pressure was chosen to be 240 mbar. There another scan of channel voltage V_{CH} and gate voltage V_{GA} as shown in figure 7.4 left. It shows the same behavior of the scan at 260 mbar. To calculate the electron potential the channel opening voltage for a corresponding gate voltage is determined and equation

$$V_{\mathrm{CH,open}} = \frac{1-\beta}{\beta} V_{\mathrm{GA,open}} - \frac{1}{\beta} V_e \,, \tag{7.1}$$

, obtained from equation 6.2, fitted to the values. The fit is plotted in red and gives the $V_e = 0.5039(82)$ V and $\beta = 0.7380(11)$. It matches well with the channel open for gate voltages lower than $V_{GA} = -1$ V. But for small gate voltages the channel opening voltage deviates strongly from

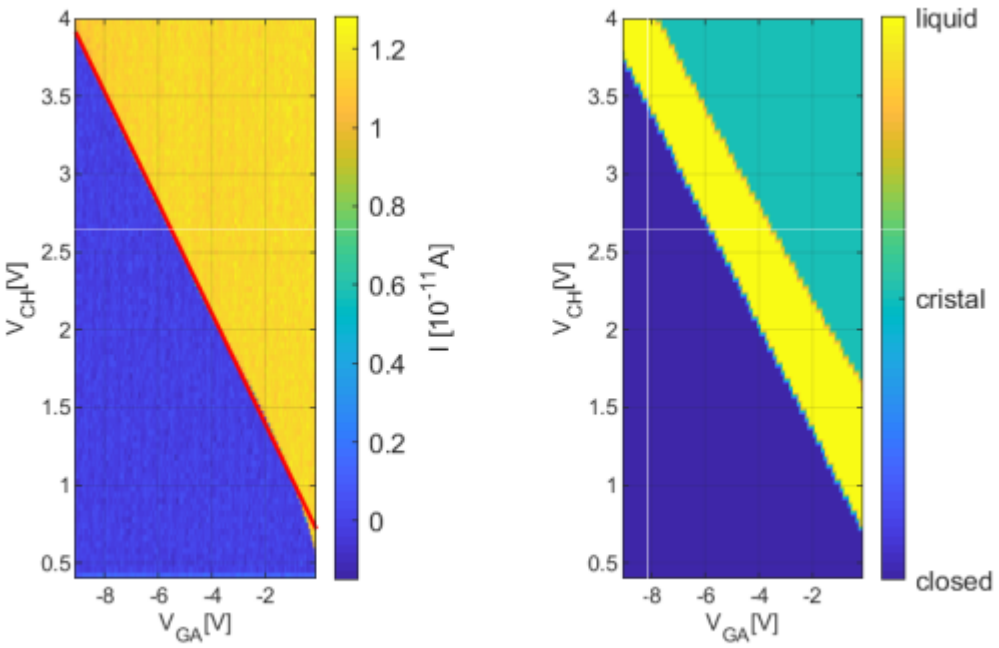

Figure 7.4: Scan of V_{GA} and V_{CH} at 260 mbar **and the expected configuration according to FEM simulation:** The current I dependent on the V_{GA} and V_{CH} is shown left. The red line shows a fit of the channel opening, which determines the electron potential $V_e = 0.5039(82)\,\mathrm{V}$. This electron potential is used to calculate the average electron density. For high densities the electrons should crystallize and the current should drop. This is not visible in the measurement.

the fit. It is not linear anymore, but the needed channel voltage is decreasing fast.

With the obtained electron potential the average electron density for set channel V_{CH} and gate voltages V_{GA} is calculated. If $V_e > \Phi_0$ the channel is closed and therefore the electron density in the channel is zero. For lower V_e the channel is open and the electron density increases. At a fixed average density the electrons should crystallize leading to a drop in current. That expected drop is shown in figure 7.4 right. According to the values obtained in the simulation the electrons should crystallize in the scanned region.

Therefore we conclude that the electron density in the reservoirs is very low and does not support a high electron density in the central channel. This is also supported by the deposition behavior. Previous samples with a similar design showed, if they supported high electron densities, no pick-up current, but just an increase of the current to a fixed value as the filament is fired. The maximum current did not depend on the time the filament was fired. But in this sample, the current shows the pick-up and then decreases to a value above the background. Even at 0.6 K, where the density needed to see the Wigner crystallization is lower, it is not present. Additionally, the deviation of the channel opening voltages for low gate voltages V_{GA} can be explained by this. For low gate voltages the effective width of the channel is very wide even for $V_e \lessapprox \Phi_0$ and it, therefore, takes many electron to fill the channel. This is not possible due to the low density in the reservoirs, which would increase the electron potential V_e there.

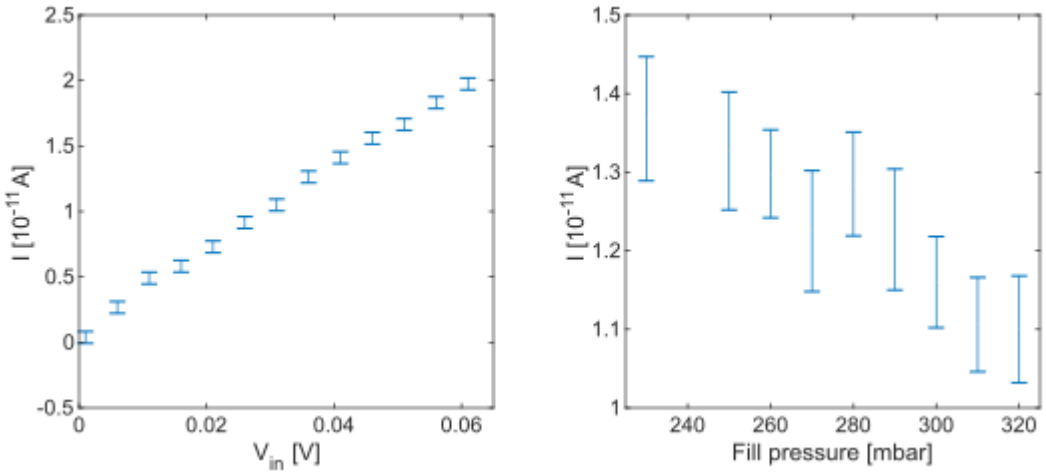

Figure 7.5: Current dependent on driving voltage and filling level: The current of the electron system increases linear with the driving voltage V_{in} at $V_{\text{CH}} = 4\,\text{V}$ and $V_{\text{GA}} = -9\,\text{V}$, where Wigner-crystallization is expected. As the driving voltage is linear, this is not observed. The mean current through the central channel taken from the Scan of V_{GA} and V_{CH}, partially shown in figure 9.6 at different filling pressures/ levels. With increasing filling level the mean current decreases due to an increased distance between electrons and the reservoir electrodes leading to a smaller capacitive coupling.

To confirm that the electrons are not in the sliding regime of the Wigner crystal due to a too high driving voltage V_{in}, the driving voltage is varied from 0 V up to 0.06 V for $V_{\text{CH}} = 4\,\text{V}$ and $V_{\text{GA}} = -9\,\text{V}$. The current increases linearly with the driving voltage and therefore the electrons are not crystallized.

To investigate the dependence of the current on the filling level the mean current for the open channel at different filling levels is calculated. The uncertainty is due to the standard deviation of the mean value. Some additional scans of V_{GA} and V_{CH} are shown in the appendix graphic 9.6. Overall the current decreases with increasing filling level. This can be explained by a decreased capacitive coupling due to increased distance between the electrons and the reservoir electrodes, leading to a smaller capacitance. This indicates that the electron density stays approximately constant independent from the filling level.

As both samples were from the same batch and showed no defects under an optical microscope, the difference in the behavior cannot be explained. To investigate this further, the samples are compared in the SEM. Also this showed no difference between the two samples.

In summary, the deposition of electrons onto the helium surface in the channels is demonstrated. Basic control of the electron system such as channel opening and closing due to changes of V_{GA} and V_{CH} is possible. Additionally, the electrons trapped in the device are stable for time periods longer than 8 h and do not break through up to a channel voltage $V_{\text{CH}} = 10\,\text{V}$. Wigner crystallization was not observed.

7.2 Second Cool-Down

In the second cool-down the first sample was mounted onto the PCB and put into the cell described in 5.3.1, while for the second sample the existing cell was used. Due to a low temperature leak

in the first cell, this sample cell was not used in the experiment. The sample in the existing cell showed a pick-up current similar to the previous samples and it was also possible to deposit electrons onto the surface.

7.2.1 Sample 1

As the cell of sample 1 showed a leak at low temperature, it was not filled with liquid He. Anyway, the filament mounted on the PCB was tested and showed a glow emission detectable at the right reservoir. Therefore the design is with the connector for the filament soldered on the PCB is working.

7.2.2 Sample 2

The deposition of electrons on sample 2 is similar to sample 2 in the first cool-down. As soon as the filament is fired a pick-up is visible and then goes down to a current above the background current. This current is higher than in the previous device. Accordingly we expect a higher electron density in the reservoirs.
Increasing the channel voltage above 3.3 V , in contrast to the previous sample, leads to a decrease in the current. This decrease is, dependent on the applied voltage, only partially reversible or even leads to a permanent decrease of the current to the background current until the surface is charged again. This indicates that the He surface in the central channel only supports a limited electron density. Above that critical electron density the electrons break through and get lost in the channel electrode. Increasing the filling level does not increase the channel voltage at which the break through appears. Therefore, I expect that some dust or sharp tip in the central channel causes this behavior. Pictures taken in the SEM do not confirm this expectation. The central channel shows no sharp tips (see figure 7.7).
Also the scan of V_{GA} and V_{CH} differs from the previous sample. A pinch off appears for a critical gate voltage $V_{\mathrm{GA,\ pinch\text{-}off}}$. For gate voltage $V_{\mathrm{GA}} < V_{\mathrm{Ga,\ pinch\ off}}$ the channel cannot be opened by increasing the channel voltage. This pinch off voltage changes with the filling level, but shows no clear dependence. Also in this sample the Wigner crystallization is not visible. As the electron potential is similar to the one in figure 7.4, one can see that the crystallization also should take also place in the scanning range chosen in figure 7.6 a), d).
The break-through of electrons is used to realize the scan of V_{GA} and V_{CH} at different electron densities. Therefore, the surface is charged up to the maximum supported electron density and then the voltage is increased above 3.3 V to cause a break-through of electrons to the channel electrode. Then the voltage is reduced below the break through voltage. The current decreases, because the electron density in the reservoirs is reduced and therefore the capacitive coupling decreases. The scans of V_{GA} and V_{CH} with different electron densities in the reservoirs are done at a filling level of 250 mbar and are shown in figure 7.6 a), b) and c) with decreasing electron density. One can clearly see an overall current decrease with decreased electron density. Additionally a decreased current for high channel voltages is visible. This decrease can be explained by a decreased electron number in the reservoir due to the increase of electrons in the channel. Especially for a low electron density in the reservoir a substantial number of electrons can be moved into the central channel.

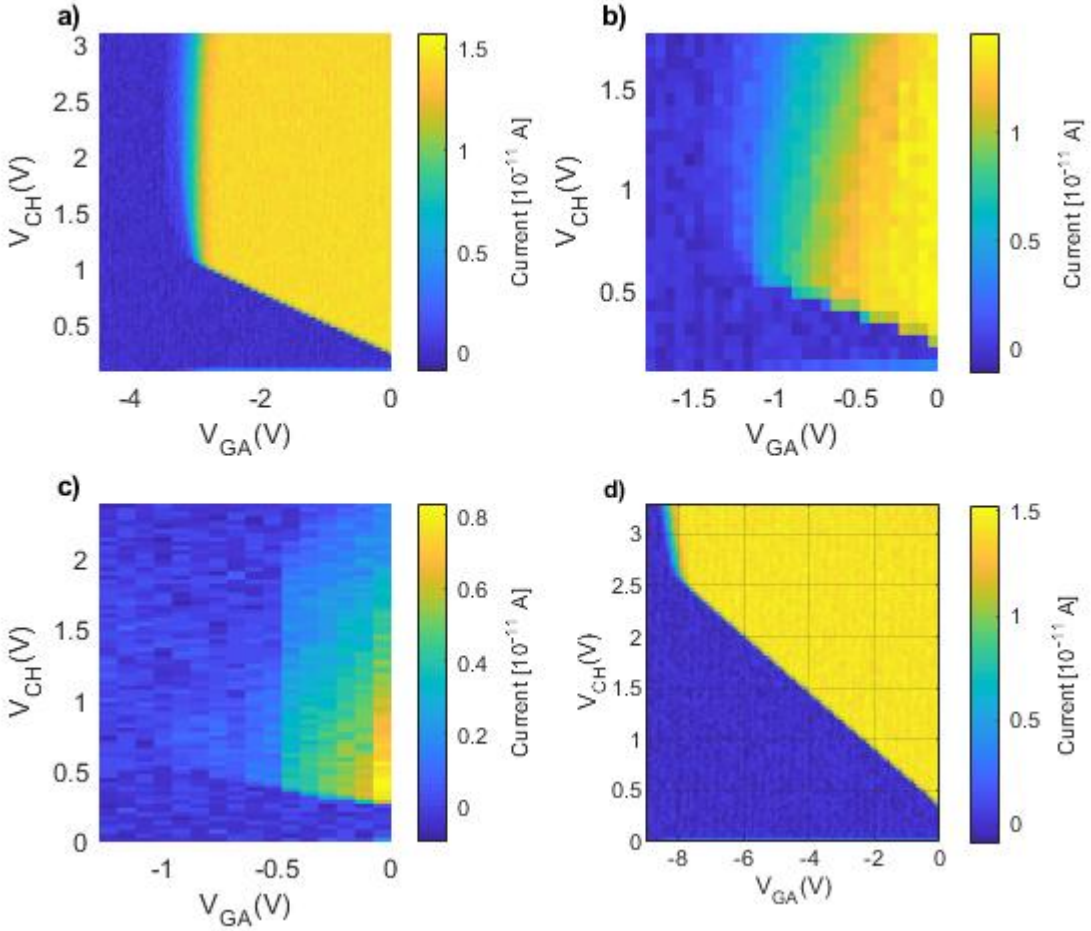

Figure 7.6: Scan of V_{GA} and V_{CH} at different filling level and electron densities: a) Scan at 250 mbar with the maximum supported electron density. Compared to the previous samples a pinch-off is visible now. Below a certain V_{GA} it is not possible to open the channel by increasing the V_{CH}**b)** Scan at 250 mbar with lower density. **c)** Scan at 250 mbar with reduced electron density. **d)** Scan at 270 mbar with the maximum supported electron density.

At one point the density in the reservoir is so low that the capacitive coupling and therefore the current decreases.

After warming up the fridge the device is analyzed in the SEM. Some pictures are shown in 7.7. There a shift of the central channel compared to the channel electrode is visible. This is not intended and different to the previous samples. Therefore, the potential distribution in the central channel is modified and could lead to the measured pinch-off. The limited electron density in the central channel cannot be explained by defects or residues in it. The largest dirt particle in the central channel is approximately 100 nm big. However, it is not clear whether this particle was on the surface before cooling down or got there after warming up. In the reservoir one can see some gold flakes that broke off from the guard electrode. These could lead to a local decrease in the film thickness, limiting the electron density in the reservoirs.

In summary, we can conclude that it is possible to deposit electrons to the He surface in the 20 µm wide and 4.38(10) µm deep channels. High electron density in the central channel leading

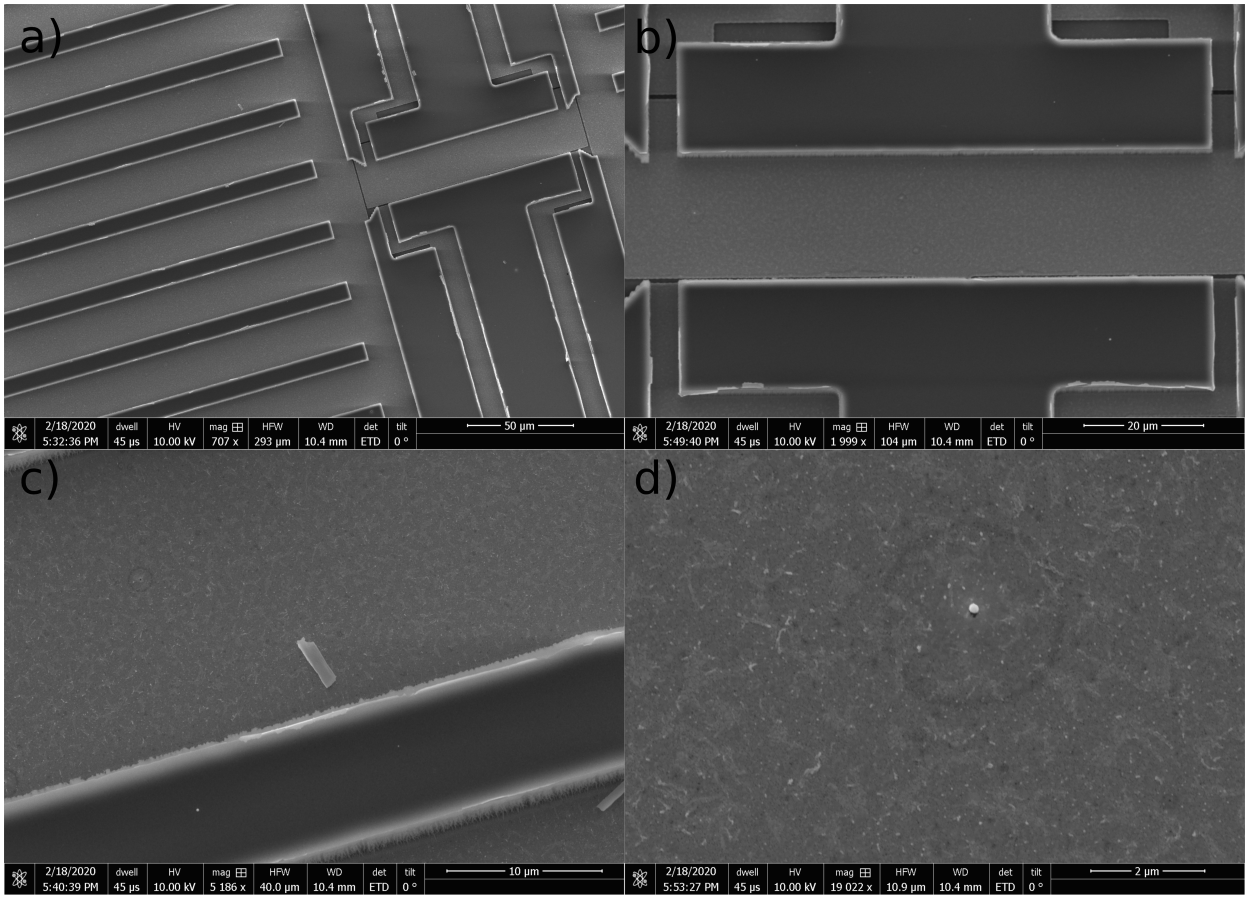

Figure 7.7: SEM images of testsample 2, cool-down 2: The central channel is smooth without any sharp objects that could lead to the break-through of electrons. The biggest object found in the channel is a dust particle shown in d), with size of approximately 100 nm. However, in the reservoir are some metal parts visible that broke off from the top electrode (c)). This could explain the limited electron density. Compared to previous samples the central channel is shifted and not centered above the channel electrode. This leads to a modified potential distribution and could cause the pinch-off.

to Wigner crystallization was not achieved. The behavior between samples of different batches varies, but can be explained by a shift of the central channel compared to the channel electrode in one sample.

7.3 Third Cool-Down

The third cool-down was done in the dilution refrigerator reaching a base temperature of 100 mK. There the new cell body with the He filling line at the side was mounted onto the mixing chamber plate and connected with the wave guide to perform the measurement with microwaves. Across from the microwave inlet a bolometer is placed to detect the microwave power inside the cell.
The cell was filled two times with helium, but showed, analogous the sample 1 in the first cool-down only a pick-up, but no electron current. Therefore no measurements with of the Rydberg excitation of the electrons with microwaves could be performed.

8 Conclusion and Outlook

In this work, I developed a FEM model of the channel to calculate the electron density and holding field in the central channel. In this model, in contrast to the previous models, the depression of the He film in the central channel is considered. Based on this, the scaling behavior of the holding field with the channel width, depth and depression is analyzed. The holding field in the experiment is restricted by the frequency $f = 400\,\mathrm{GHz}$ of the microwave source to $1000\,\mathrm{V\,cm^{-1}}$. The scaling behavior of the holding field with the channel depth d is comparable with a parallel-plate capacitor, but interestingly the holding field is reduced by the channel structure. The channel width W has up to 20 µm a negligible influence on the holding field. For wider channels the holding field increases fast due to the W^2 scaling of the depression. The depression of the helium film increases overall the holding field due to a reduced distance between electrons and channel electrode, but more interestingly, it modifies the electric field distribution across the channel. It leads to homogenous holding fields across the channel for the right combination of channel voltage V_{CH}, gate voltage V_{GA} and electron potential V_e. The constant holding field in the channel is needed to achieve the excitation of a large number of electrons. From the simulation a channel width of 20 µm and depth of 4 µm is determined to be suited for the experiment. The calculations also showed that the implementation of the image charge detection using the channel electrode is possible.
Besides the simulations, a sample cell with microwave inlets is designed. Also a PCB as sample holder is designed. To fabricate a sample with 20 µm wide and 4 µm deep channels the depence of the thickness on the spin rate of the ARN 4450-10 photoresist are analyzed, as well as the chemical stability against the solvents and developer used in later steps of the fabrication. Based on this, the sample preparation is optimized for the photoresist ARN 4450-10.
With the fabricated samples the deposition of surface electrons in the channels is demonstrated. Basic control over the electron system is demonstrated such as opening and closing the central channel by the gate voltage V_{GA} and channel voltage V_{CH}. Wigner crystallization is not observed. With this work I laid the ground work for the detection of the Rydberg-excitation of electrons in micro channels.
In future work, after demonstrating the detection of the Rydberg-excitation of electrons in microchannels using the current design, the channels should be scaled down. According to the higher holding field microwave sources with a higher frequency should be used. In smaller channels single rows of electrons can be set up and therefore the influence of the Rydberg-excitation on the transport behavior in 1D could be observed. Additional to the transport measurement, the image charge detection can be implemented as another possibility to observe the Rydberg-excitation. Besides that one could use a magnetic material for the top layer to create a magnetic field gradient in a outer magnetic field. With this magnetic field gradient spin dependent Rydberg-excitation of the electrons can be realized due to a different Zeeman-splitting between the ground state and the

first exited state.

List of Figures

Bibliography

[1] F. et al. Arute. Quantum supremacy using a programmable superconducting processor. *Nature*, 574:505–510, 10 2019. doi: 10.1038/s41586-019-1666-5.

[2] P. M. Platzman and M. I. Dykman. Quantum computing with electrons floating on liquid helium. *Science*, 284(5422):1967–1969, 1999. ISSN 0036-8075. doi: 10.1126/science.284.5422.1967. URL `https://science.sciencemag.org/content/284/5422/1967`.

[3] D. I. Schuster, A. Fragner, M. I. Dykman, S. A. Lyon, and R. J. Schoelkopf. Proposal for manipulating and detecting spin and orbital states of trapped electrons on helium using cavity quantum electrodynamics. *Phys. Rev. Lett.*, 105:040503, Jul 2010. doi: 10.1103/PhysRevLett.105.040503. URL `https://link.aps.org/doi/10.1103/PhysRevLett.105.040503`.

[4] C. C. Grimes, T. R. Brown, Michael L. Burns, and C. L. Zipfel. Spectroscopy of electrons in image-potential-induced surface states outside liquid helium. *Phys. Rev. B*, 13:140–147, Jan 1976. doi: 10.1103/PhysRevB.13.140. URL `https://link.aps.org/doi/10.1103/PhysRevB.13.140`.

[5] W. T. Sommer. Liquid helium as a barrier to electrons. *Phys. Rev. Lett.*, 12:271–273, Mar 1964. doi: 10.1103/PhysRevLett.12.271. URL `https://link.aps.org/doi/10.1103/PhysRevLett.12.271`.

[6] Boyce Burdick. Negative ions in liquid helium ii. *Phys. Rev. Lett.*, 14:11–13, Jan 1965. doi: 10.1103/PhysRevLett.14.11. URL `https://link.aps.org/doi/10.1103/PhysRevLett.14.11`.

[7] C. C. Grimes and Gregory Adams. Observation of two-dimensional plasmons and electron-ripplon scattering in a sheet of electrons on liquid helium. *Phys. Rev. Lett.*, 36:145–148, Jan 1976. doi: 10.1103/PhysRevLett.36.145. URL `https://link.aps.org/doi/10.1103/PhysRevLett.36.145`.

[8] Jui-Yin Lin. *Transport properties of strongly correlated 2D electrons confined in microchannels*. PhD thesis, Okinawa Institute of Science and Technology Graduate University, September 2018.

[9] David Lambert. *ELECTRONS ON THE SURFACE OF LIQUID HELIUM*. PhD thesis, Lawrence Berkeley National Laboratory, University of California, May 1979.

[10] Kimitoshi Kono Yuriy Monarkha. *Two-Dimensional Coulomb Liquids and Solids*. Springer Science & Business Media, Berlin, Heidelberg, 2013. ISBN 978-3-662-10639-6.

[11] K. Shirahama, S. Ito, H. Suto, and K. Kono. Surface study of liquid ^{3}he using surface state electrons. *Journal of Low Temperature Physics*, 101(3):439–444, Nov 1995. ISSN 1573-7357. doi: 10.1007/BF00753334. URL https://doi.org/10.1007/BF00753334.

[12] Motohiko Saitoh. Warm electrons on the liquid ^{4}he surface. *Journal of the Physical Society of Japan*, 42(1):201–209, 1977. doi: 10.1143/JPSJ.42.201.

[13] Laurence Lurio, T. Rabedeau, Peter Pershan, and Isaac Silvera. X-ray specular reflectivity of the 4he liquid-vapor interface. *Physica B-condensed Matter - PHYSICA B*, 169:507–508, 02 1991. doi: 10.1016/0921-4526(91)90299-T.

[14] Takayuki Aoki and Motohiko Saitoh. Theory of hot electrons on the liquid 4he surface ii. *Journal of the Physical Society of Japan*, 46(2):423–431, 1979. doi: 10.1143/JPSJ.46.423.

[15] Tsuneya Ando. Broadening of inter-subband transitions in image-potential-induced surface states outside liquid helium. *Journal of the Physical Society of Japan*, 44(3):765–773, 1978. doi: 10.1143/JPSJ.44.765.

[16] A. P. Volodin and V. S. Edel'ma. Photoresonance and mobility of electrons localized over liquid helium. *Journal of Experimental and Theoretical Physics*, 54:198–205, 06 1981.

[17] Denis Konstantinov, Kimitoshi Kono, and Yuriy Monarkha. Photoresonance and conductivity of surface electrons on liquid 3he. *Low Temperature Physics - LOW TEMP PHYS*, 34:377–384, 04 2008. doi: 10.1063/1.2911657.

[18] Denis Konstantinov, Hanako Isshiki, Yuriy Monarkha, Hikota Akimoto, Keiya Shirahama, and Kimitoshi Kono. Microwave-resonance-induced resistivity: Evidence of ultrahot surface-state electrons on liquid ^{3}He. *Phys. Rev. Lett.*, 98:235302, Jun 2007. doi: 10.1103/PhysRevLett.98.235302. URL https://link.aps.org/doi/10.1103/PhysRevLett.98.235302.

[19] E. Wigner. On the interaction of electrons in metals. *Phys. Rev.*, 46:1002–1011, Dec 1934. doi: 10.1103/PhysRev.46.1002. URL https://link.aps.org/doi/10.1103/PhysRev.46.1002.

[20] J M Kosterlitz and D J Thouless. Long range order and metastability in two dimensional solids and superfluids. (application of dislocation theory). *Journal of Physics C: Solid State Physics*, 5(11):L124–L126, jun 1972. doi: 10.1088/0022-3719/5/11/002. URL https://doi.org/10.1088%2F0022-3719%2F5%2F11%2F002.

[21] J M Kosterlitz and D J Thouless. Ordering, metastability and phase transitions in two-dimensional systems. *Journal of Physics C: Solid State Physics*, 6(7):1181–1203, apr 1973. doi: 10.1088/0022-3719/6/7/010. URL https://doi.org/10.1088%2F0022-3719%2F6%2F7%2F010.

[22] A. P. Young. Melting and the vector coulomb gas in two dimensions. *Phys. Rev. B*, 19:1855–1866, Feb 1979. doi: 10.1103/PhysRevB.19.1855. URL https://link.aps.org/doi/10.1103/PhysRevB.19.1855.

[23] C. C. Grimes and G. Adams. Evidence for a liquid-to-crystal phase transition in a classical, two-dimensional sheet of electrons. *Phys. Rev. Lett.*, 42:795–798, Mar 1979. doi: 10.1103/PhysRevLett.42.795. URL https://link.aps.org/doi/10.1103/PhysRevLett.42.795.

[24] M. I. Dykman, C. Fang-Yen, and M. J. Lea. Many-electron transport in strongly correlated nondegenerate two-dimensional electron systems. *Phys. Rev. B*, 55:16249–16271, Jun 1997. doi: 10.1103/PhysRevB.55.16249. URL https://link.aps.org/doi/10.1103/PhysRevB.55.16249.

[25] F. R. Bradbury, Maika Takita, T. M. Gurrieri, K. J. Wilkel, Kevin Eng, M. S. Carroll, and S. A. Lyon. Efficient clocked electron transfer on superfluid helium. *Phys. Rev. Lett.*, 107:266803, Dec 2011. doi: 10.1103/PhysRevLett.107.266803. URL https://link.aps.org/doi/10.1103/PhysRevLett.107.266803.

[26] D. G. Rees, I. Kuroda, C. A. Marrache-Kikuchi, M. Höfer, P. Leiderer, and K. Kono. Point-contact transport properties of strongly correlated electrons on liquid helium. *Phys. Rev. Lett.*, 106:026803, Jan 2011. doi: 10.1103/PhysRevLett.106.026803. URL https://link.aps.org/doi/10.1103/PhysRevLett.106.026803.

[27] D. Rees, Isao Kuroda, Claire Akiko Marrache-Kikuchi, Moritz Hofer, Paul Leiderer, and Kimitoshi Kono. Transport measurements of strongly-correlated electrons on helium in a classical point-contact device. *Journal of Low Temperature Physics*, 50, 05 2011. doi: 10.1007/s10909-011-0416-3.

[28] Hiroki Ikegami, Hikota Akimoto, and Kimitoshi Kono. Melting of a quasi-one-dimensional wigner crystal: Electrons on superfluid ^{4}He in a narrow channel. *Phys. Rev. B*, 82:201104, Nov 2010. doi: 10.1103/PhysRevB.82.201104. URL https://link.aps.org/doi/10.1103/PhysRevB.82.201104.

[29] Hiroki Ikegami, Hikota Akimoto, D. Rees, and Kimitoshi Kono. Evidence for reentrant melting in a quasi-one-dimensional wigner crystal. *Physical review letters*, 109:236802, 12 2012. doi: 10.1103/PhysRevLett.109.236802.

[30] David G. Rees, Hiroki Ikegami, and Kimitoshi Kono. Reentrant melting of a classical quasi-one-dimensional wigner crystal on the surface of liquid helium. *Journal of the Physical Society of Japan*, 82(12):124602, 2013. doi: 10.7566/JPSJ.82.124602. URL https://doi.org/10.7566/JPSJ.82.12460.

[31] David G. Rees, Niyaz R. Beysengulov, Juhn-Jong Lin, and Kimitoshi Kono. Stick-slip motion of the wigner solid on liquid helium. *Phys. Rev. Lett.*, 116:206801, May 2016. doi: 10.1103/PhysRevLett.116.206801. URL https://link.aps.org/doi/10.1103/PhysRevLett.116.206801.

[32] A. O. Badrutdinov, A. V. Smorodin, D. G. Rees, J. Y. Lin, and D. Konstantinov. Nonlinear transport of the inhomogeneous wigner solid in a channel geometry. *Phys. Rev. B*, 94:195311, Nov 2016. doi: 10.1103/PhysRevB.94.195311. URL https://link.aps.org/doi/10.1103/PhysRevB.94.195311.

[33] Hiroki Ikegami, Hikota Akimoto, and Kimitoshi Kono. Nonlinear transports of electrons on liquid4he in a 1.6 μm channel. *Journal of Physics: Conference Series*, 400(1):012020, dec 2012. doi: 10.1088/1742-6596/400/1/012020. URL https://doi.org/10.1088%2F1742-6596%2F400%2F1%2F012020.

[34] BlueFors Cryogenics. Bf-ld400, cryogenic free dilution refrigerator system user manual, 01 2011.

[35] D Marty. Stability of two-dimensional electrons on a fractionated helium surface. *Journal of Physics C: Solid State Physics*, 19(30):6097–6104, oct 1986. doi: 10.1088/0022-3719/19/30/019. URL https://doi.org/10.1088%2F0022-3719%2F19%2F30%2F019.

[36] Jürgen Klier, Andreas Würl, Paul Leiderer, Giampaolo Mistura, and Valeri Shikin. Cyclotron resonance for two-dimensional electrons on thin helium films. *First publ. in: Physical Review B 65 (2002), Article 165428*, 65, 04 2002. doi: 10.1103/PhysRevB.65.165428.

[37] Niyaz Beysengulov, D. Rees, Yury Lysogorskiy, N. Galiullin, A. Vazjukov, D. Tayurskii, and Kimitoshi Kono. Structural transitions in a quasi-1d wigner solid on liquid helium. *Journal of Low Temperature Physics*, 182, 10 2015. doi: 10.1007/s10909-015-1344-4.

[38] Erika Kawakami, Asem Elarabi, and Denis Konstantinov. Image-charge detection of the rydberg states of surface electrons on liquid helium. *Phys. Rev. Lett.*, 123:086801, Aug 2019. doi: 10.1103/PhysRevLett.123.086801. URL https://link.aps.org/doi/10.1103/PhysRevLett.123.086801.

[39] W. Shockley. Currents to conductors induced by a moving point charge. *Journal of Applied Physics*, 9(10):635–636, 1938. doi: 10.1063/1.1710367.

[40] S. Ramo. Currents induced by electron motion. *Proceedings of the IRE*, 27(9):584–585, Sep. 1939. ISSN 2162-6634. doi: 10.1109/JRPROC.1939.228757.

9 Appendix

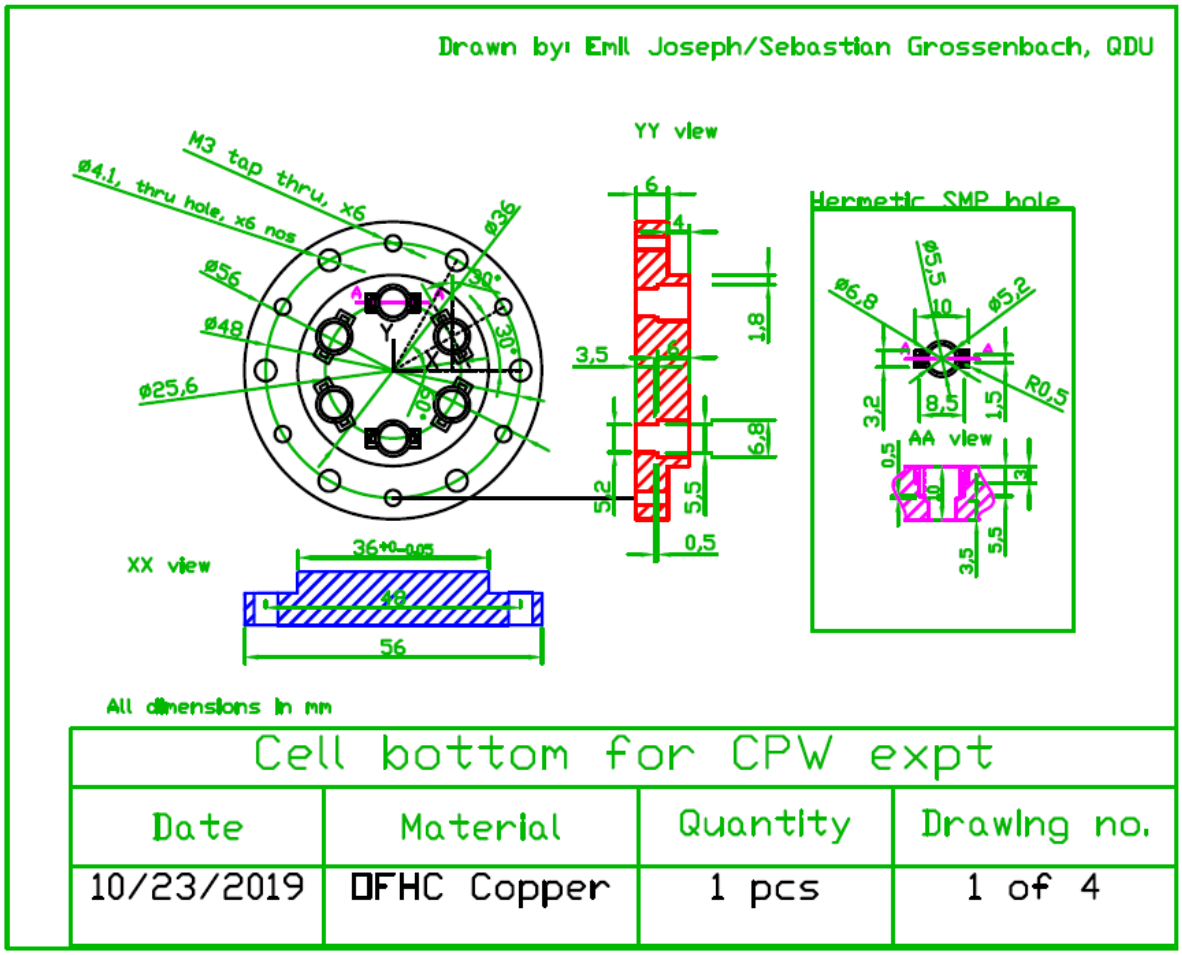

Figure 9.1: Cell Bottom

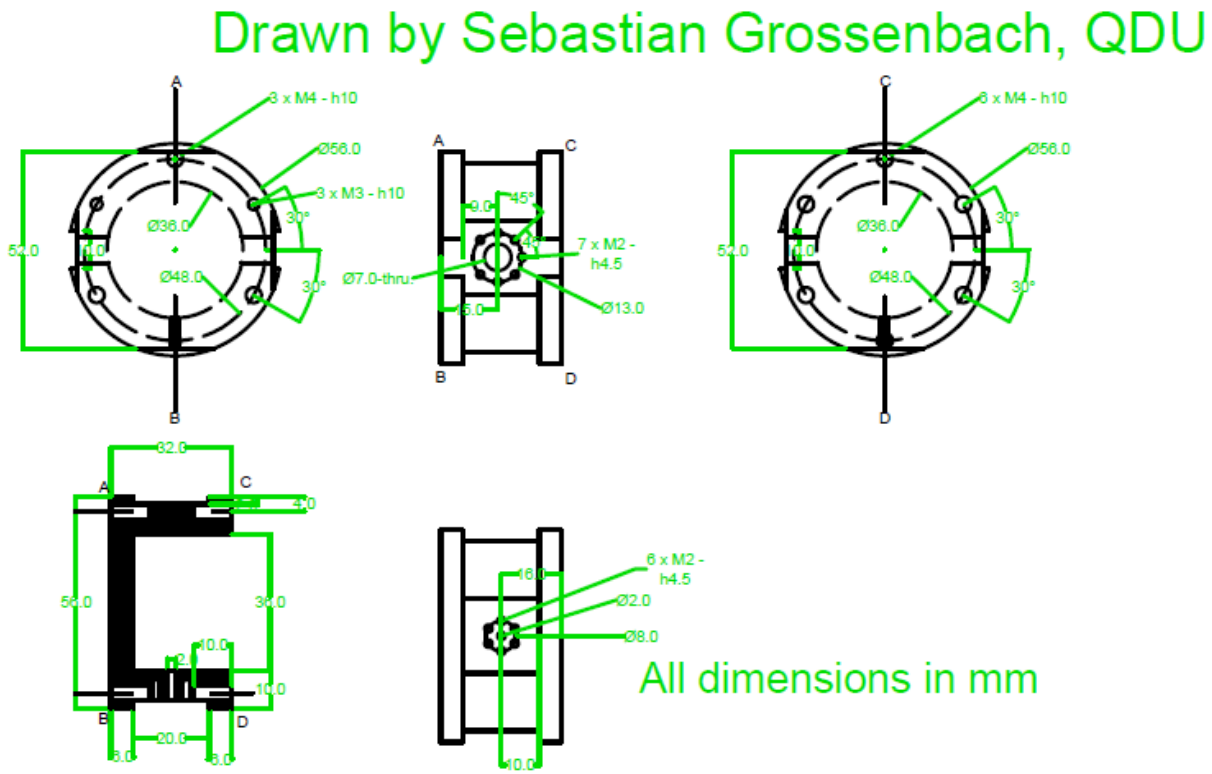

Cell Top Helium Inlet Sideways			
Date	Material	Quantity	Drawing No.
10/23/2019	OFHC Copper	1 pcs	2 of 4

Figure 9.2: Cell Body with filling line at top

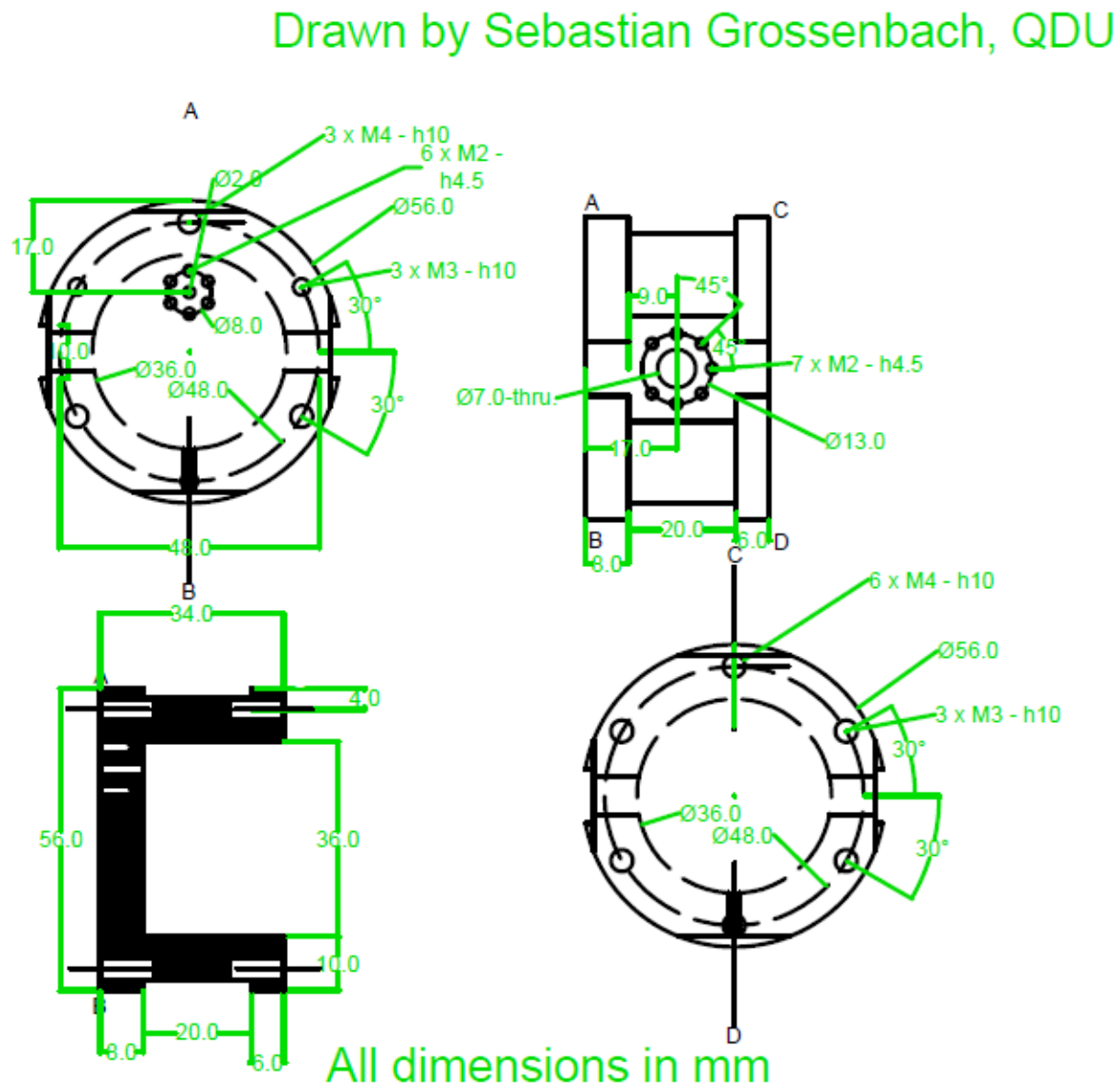

Figure 9.3: Cell Body with filling line at the side top

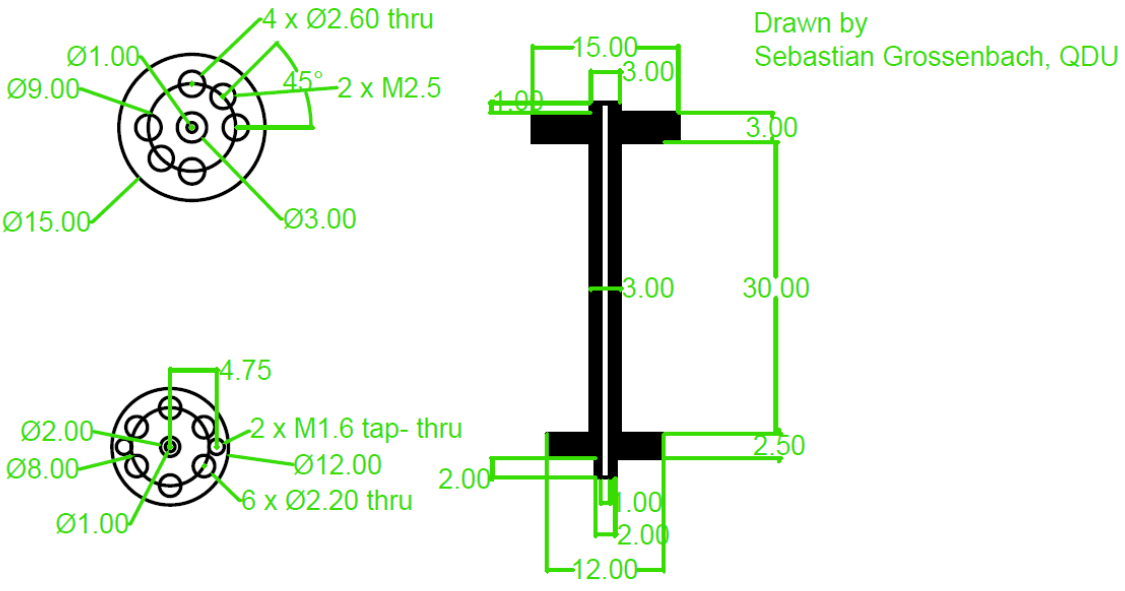

Helium filling line addapter			
Date	Material	Quantity	No. of drawing
10/19/2028	OFHC Copper	1 pcs	4 of 4

Figure 9.4: Adapter for filling line in different fridges

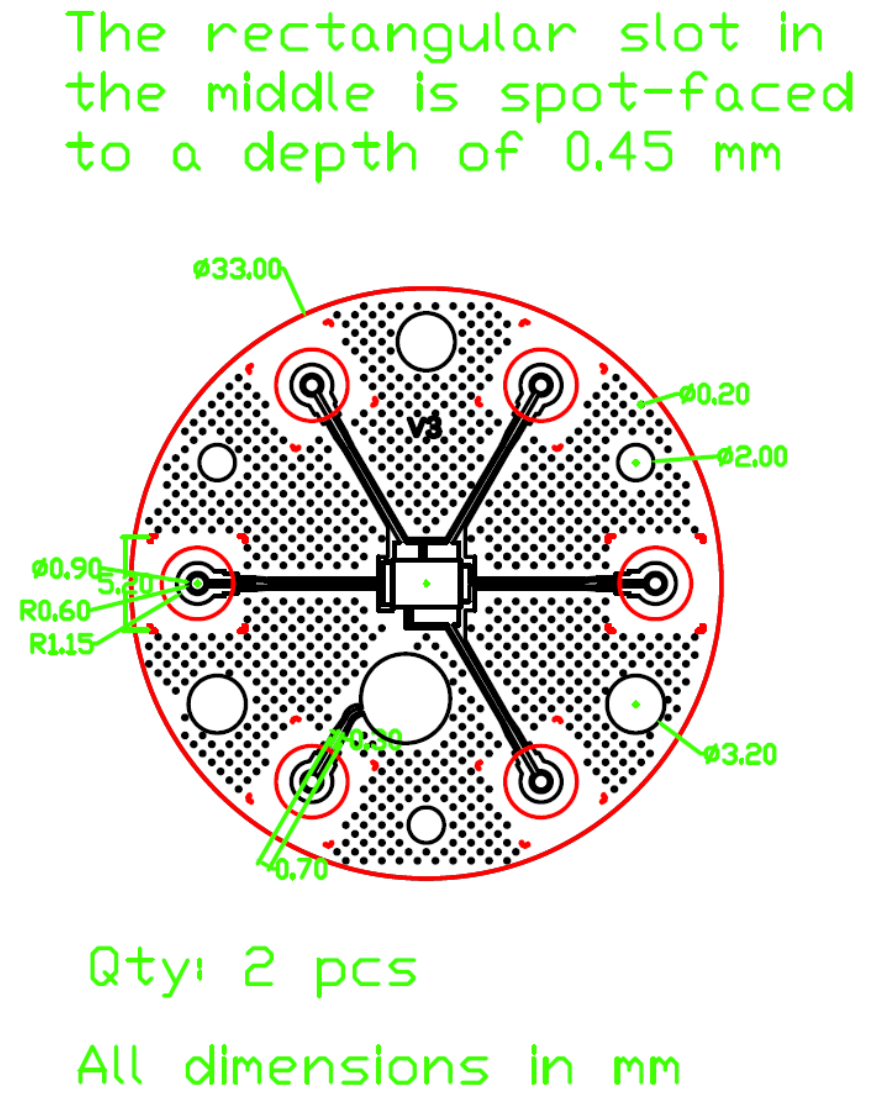

Figure 9.5: PCB

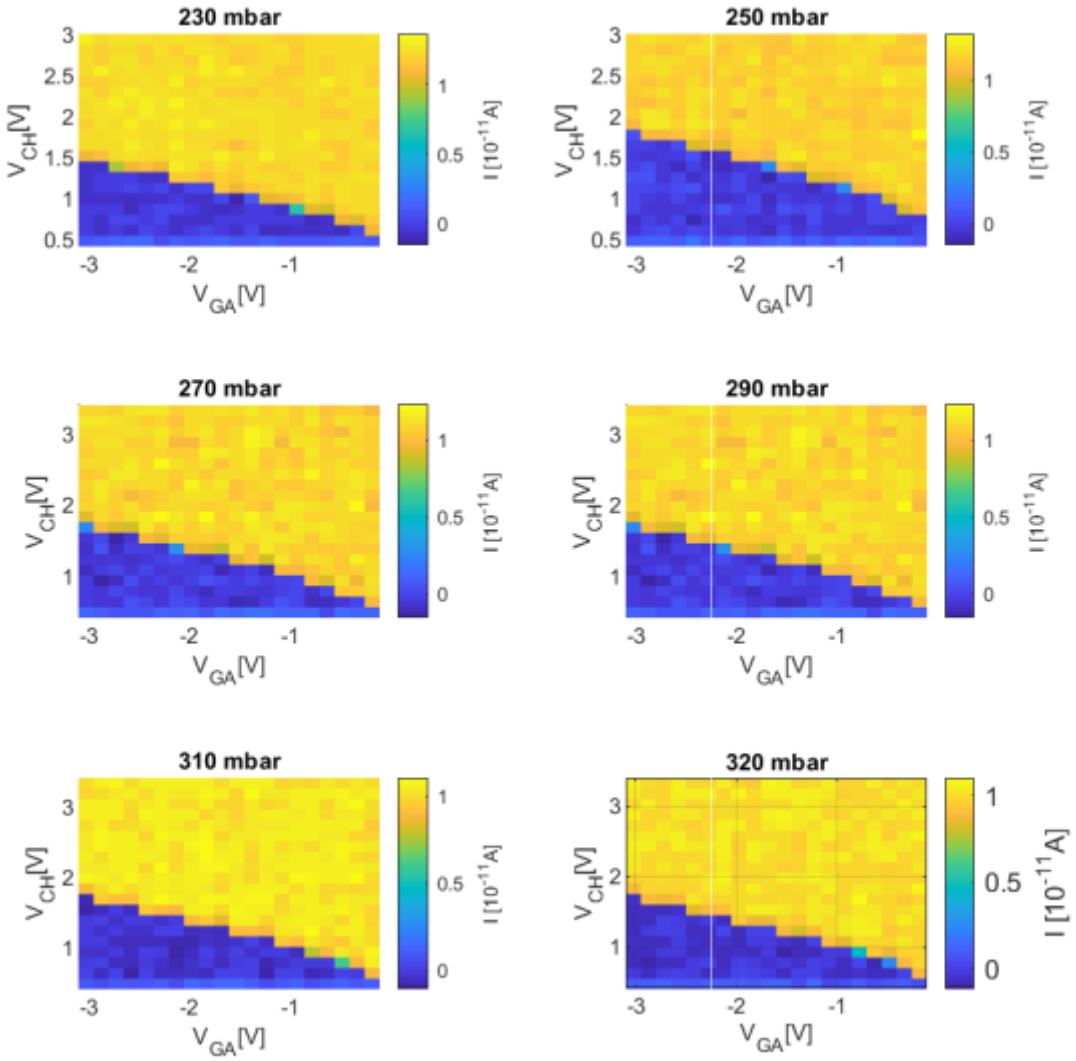

Figure 9.6: Scan of gate and channel voltage for testsample 2 over various filling levels: